Oceanologia, uncorrected, in press
Polish Academy of Sciences
Institute of Oceanology

https://doi.org/10.5697/...

Coupled current-wave simulation reveals sea surface heat fluxes responses to diurnal skin sea surface temperature modulation in the Sunda Strait

Eko Supriyadi[1,2], Tania June[1,*], Agus Saleh Atmadipoera[3], Andri Ramdhani[4]

Abstract

The Sunda Strait, a critical interoceanic conduit between the Pacific and Indian Oceans, exhibits a unique relationship between the skin SST (T_s) and the sea surface energy balance. This study aims to model the cool skin (ΔT_c) and warm layer (ΔT_w) using a coupled Regional Ocean Modeling System (ROMS) and the Simulating WAves Nearshore (SWAN) model. The focus is on analyzing the characteristics of ΔT_c and ΔT_w, quantifying the diurnal variability of the ΔT_c, developing a correction of the bulk SST (T_b) to T_s, and analyzing the sea surface energy balance relative to T_s. Results show that the ΔT_c layer contributes an average cooling of -0.2°C that varies diurnally and increases with wind speed (U_{10}) up to 8 m s^{-1} and stabilizes near -0.1°C. A two-step correction based on U_{10} and the diurnal cycle was applied to minimize the discrepancy between T_b and T_s, successfully eliminating the combined influence of ΔT_c and ΔT_w (ΔT_{cw}). Compared to other models, the proposed model shows a high correlation between ΔT_{cw} and U_{10} in the Indian Ocean, Sunda Strait, and Java Sea of 0.69, 0.74, and 0.88, respectively. This study also shows that T_s has an ocean regimes and seasonal relationship context with U_{10}, net shortwave flux (R_{sw}), net longwave flux (R_{lw}), net sensible heat flux (R_{shf}), and net latent heat flux (R_{lhf}). These findings establish T_s as a critical diagnostic parameter for understanding air-sea fluxes in tropical strait systems.

Keywords

Skin SST; Wind speed; Sea surface energy balance; Sunda Strait; ROMS; SWAN

[1] *Department of Geophysics and Meteorology, Faculty of Mathematics and Natural Sciences, IPB University, Darmaga, Bogor, 16680, Indonesia*
[2] *Marine Meteorology Center, BMKG, Kemayoran, Jakarta, 10610, Indonesia*
[3] *Department of Marine Science and Technology, Faculty of Fisheries and Marine Science, IPB University, Darmaga, Bogor, 16680, Indonesia*
[4] *Public Meteorology Center, BMKG, Kemayoran, Jakarta, 10610, Indonesia*

***Correspondence**: taniajune@apps.ipb.ac.id (T. June)

Received: 1 September 2025; **revised:** 7 December 2025; **accepted**: 23 January 2026

1. Introduction

Air-sea fluxes occur at the atmosphere-ocean interface through three primary mechanisms: heat exchange, freshwater transfer, and momentum exchange (Yu, 2018). Heat exchange near the ocean surface includes R_{sw}, R_{lw}, R_{shf}, and R_{lhf} from the heating and cooling of the lower atmosphere (Cronin et al., 2019). The primary variable governing the exchange of heat and momentum between the atmosphere and ocean is the Sea Surface Temperature (SST). Donlon et al. (2002) categorize SST into distinct levels. The first level is T_s, located at approximately 500 μm, which serves as the thermal exchange boundary between the ocean and the atmosphere, where conductive and diffusive heat exchange processes prevail. The second level, subskin SST ($T_{subskin}$), occurs at around 1 mm, characterized by dominant molecular and viscous heat exchange processes. Finally, T_b extending up to 5 m, represents the SST utilized in conventional operational measurements, where turbulent heat exchange processes are primarily influenced by solar heating.

In the context of heat and momentum flux calculations between the ocean and atmosphere, T_s has been used to provide accurate results. However, the direct measurement of T_s is challenging and typically requires an infrared radiometer operating at wavelengths of 3–18 μm (Donlon et al., 2008; Jessup and Branch, 2008; Minnett, 2003). Conversely, T_b can be measured using conventional instruments

such as bouy, drifter or ship. T_s can be up to 0.2–0.5°C lower than T_b (Fairall et al., 1996a). The difference in T_s and T_b is due to the presence of ΔT_c and ΔT_w effects (Fairall et al., 1996a,b; Murray et al., 2000; Pimentel et al., 2019). ΔT_c occurs due to ocean friction with surface winds, which in turn is related to seawater viscosity and is 0.2°C cooler than conventional SST measurements (Saunders, 1967a). Fairall et al. (1996a) found that when wind speeds were around 1.5 m s^{-1} the ΔT_c correction gave a value of 0.35°C. On a diurnal scale, the ΔT_c effect is more prominent at night (Murray et al., 2000). The presence of shortwave flux during the day results in a warming of the sea surface known as the ΔT_w. Fairall et al. (1996a) describe this layer as stably stratified in the absence of wind-induced turbulent mixing, and its warming effect can persist long after sunset. Using a prognostic approach, Zeng and Beljaars (2005) proposed that the ΔT_w evolves with time. Given limited observational data, the coupled ROMS-SWAN model serves as the primary tool to derive ΔT_c and ΔT_w effects across the Sunda Strait.

Observations of T_s have been made in almost all types of waters of the world in recent decades with varying results. Fairall et al. (1996a) processed T_s observation data in the Western Pacific Ocean during the period 1992–1993 and found that if the combination of ΔT_c (ΔT_w) effects is ignored, it can increase (decrease) the atmospheric heat input to the ocean by 11 W m^{-2} and 4 W m^{-2}, respectively. Furthermore, Fairall et al. (1996b) explained that the ΔT_c (ΔT_w) causes cooling (warming) of about 0.1°C and several degrees Celsius, respectively. Then, Luo et al. (2022) made observations in the Caribbean Sea and obtained a ΔT_c model having a bias of −0.128°C and 0.028°C, respectively, while the ΔT_w model showed agreement with the model developed by Fairall et al. (1996a), which is 0.166°C. In tropical waters, strong ΔT_c and ΔT_w values were found by Zhang et al. (2021) in the South China Sea by 0.4°C. Meanwhile, at high latitudes, Pimentel et al., (2019) found a ΔT_c (ΔT_w) in the Mediterranean Sea of 0.8°C (−0.7°C to 2.4°C), respectively. Subsequently, Zhang et al. (2020) reported an average ΔT_c value of −0.23°C during a voyage from Australia to Antarctica, noting that this value dropped to −0.36C before dawn. In contrast, ΔT_w because it requires specific conditions, namely the sea surface receiving a high heat flux and a warmer air temperature relative to T_s. Correction of the coastal water T_s observations was also carried out by Alappattu et al. (2017) in North Carolina, which obtained a mean T_b–T_s of 0.4°C. ROMS modeling for T_s and its assimilation with satellite observations was also carried out by Iversen et al. (2023). Recently, Li et al. (2023) used the Haiyang-1D satellite to calculate global T_s based on atmospheric radiative transfer modeling. However, Iversen et al. (2023) and Li et al. (2023) did not discuss the specific ΔT_c and ΔT_w as part of the T_s. From the above references, T_s are generally obtained through observations and rarely through ocean modeling approaches.

To address this methodological gap through a modeling approach, this study focuses on the Sunda Strait. Characterized by complex air-sea processes within the dynamic Indonesian archipelago (Putri, 2005), it is a region where the interplay between intense solar insolation and varying wind speeds makes the accurate quantification of the ΔT_c and the diurnal ΔT_w particularly urgent (Fairall et al., 1996; Minnett, 2003). However, robust validation of modeled ΔT_c and ΔT_w corrections requires high-accuracy direct in situ radiometric measurements of T_s, utilizing instruments such as the Marine-Atmospheric Emitted Radiance Interferometer (M-AERI, Gentemann and Minnett, 2008; Minnett et al., 2001) or the Infrared Sea Surface Temperature Autonomous Radiometer (ISAR; Donlon et al., 2008). To date, such specialized, high-resolution T_s measurements have not been documented or deployed in the Sunda Strait to directly constrain numerical models. This study aims to utilize the ROMS-SWAN coupled model to quantify the ΔT_c and ΔT_w in correcting T_b toward the T_s. The T_s value is then integrated into the sea surface energy balance analysis, including R_{sw}, R_{lw}, R_{shf} and R_{lhf}. We only utilize the outputs of solar radiation, wind speed and T_b as the basis for deriving ΔT_c and ΔT_w. This paper is organized in several sections such as Section 2 describes the dataset and technical steps of modeling ΔT_c and ΔT_w; Section 3 presents the validation of T_b, the comparison of T_s and T_b, illustrates the characteristics of ΔT_c and ΔT_w, diurnal variability of ΔT_c, correction of ΔT_c and ΔT_w, modeling performance ΔT_{cw}, and analysis effects of T_s, U_{10} and sea surface energy balance on ocean regimes and seasonality; finally, Section 4 summarizes all the main findings.

2. Methods

2.1 Study area

This study was conducted in the Sunda Strait at coordinates (−8.5; −4)°N and (103; −108)°E with a domain rotation of 30° counter-clockwise to capture a wider water area. The spatial resolution used was 1 km with a 435×235 grid configuration to analyze the details of coastal air-sea interaction processes. For the stability model, a spin-up was applied during 2022 and then further analyzis was carried out in 2023 with a temporal resolution of 1 hour. The domain details can be seen in Figure 1.

2.2 Configuration model, flux calculation, and output

The model configuration was designed to resolve the complex circulation and mixing processes in the Sunda Strait. A stretched sigma vertical coordinate system with 50 levels was employed to enhance the resolution near the surface with $\theta_s = 10$ and $\theta_b = 0.4$. Horizontal mixing was parameterized using the harmonic (biharmonic) diffusivity for the active tracers with values of 20 (200) m^2 s^{-1} and biharmonic (harmonic) viscosity for the momentum set to 100 (250) m^4 s^{-1}, balancing computational stability with

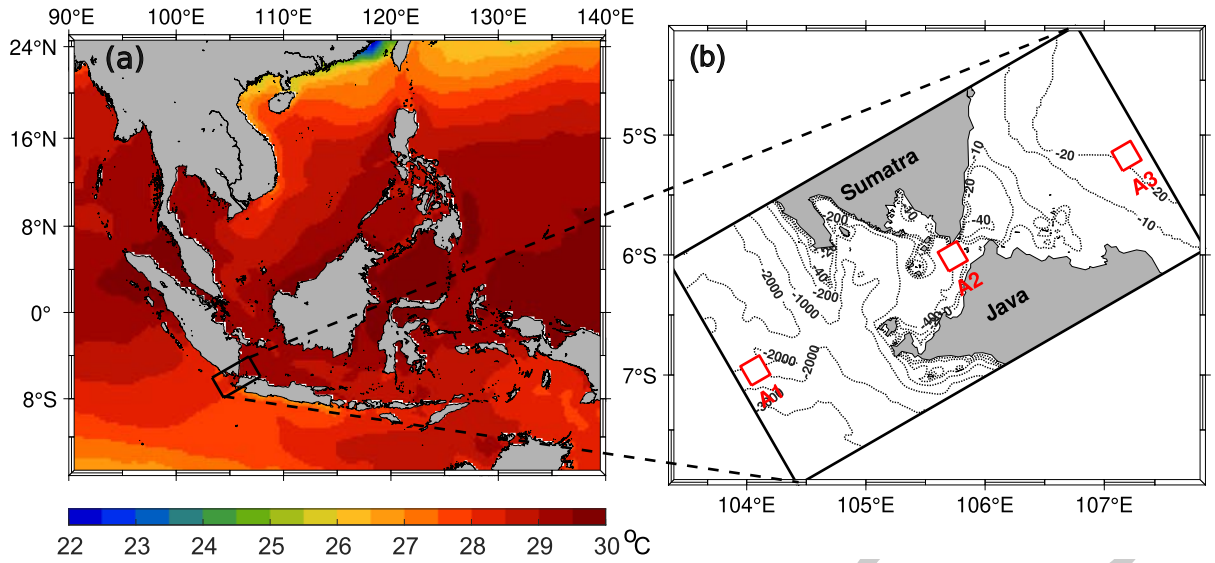

Figure 1. a) The SST of Indonesia waters for the period 2023 (Huang et al., 2021). b) Bathymetry of the Sunda Strait from General Bathymetric Chart of the Oceans (GEBCO) marked with a dashed line (in meters) and the land as a gray patch. The Sunda Strait study domain is marked with red boxes at 3 sites such as A1, A2, and A3, representing the Indian Ocean, Sunda Strait, and Java Sea, respectively. All red boxes are 20 × 20 km.

the preservation of the mesoscale dynamics. Given the region's open connection to the dynamic Indian Ocean and the shallower Java Sea, Lateral Boundary Conditions (LBCs) were carefully configured. Specifically, Chapman_explicit, Shchepetkin, Shchepetkin, Closed, and Radiation + Nudging LBCs were applied for zeta, 2D momentum, 3D momentum, TKE mixing, and tracers, respectively, to enable realistic wave propagation and water exchange while minimizing spurious boundary reflections. The model timestep was determined based on the Courant–Friedrichs–Lewy (CFL) equation (de Moura and Kubrusly, 2013):

$$dt \approx \Delta t = \frac{\min(\Delta x, \Delta y)}{\sqrt{2 \times g \times h_{\max}}} \quad (1)$$

Given our grid resolution (Δx, $\Delta y = 1$ km), gravitational acceleration ($g = 9.8$ m^2 s^{-1}) and the maximum depth ($h_{\max} \sim 5400$ m), the external mode time step was set to 3 seconds.

Wave physics were parameterized as follows: depth-induced breaking was activated with a constant breaker criterion ($\alpha = 1.0, \gamma = 0.73$), and bottom friction was represented using the MADSEN formulation with a roughness factor of 0.05. Following Komen et al. (1984), whitecapping dissipation was enabled with a dissipation coefficient C_{ds} of 2.36×10^{-5} and a wave slope s_{pm}^{-2} of 3.02×10^{-3} for the Pierson-Moskowitz spectrum. The slope power is defined as powst = 2, while the whitecapping coefficient at the wave number is designated as delta = 1. The wave number power is then normalized by the mean wave number (powk = 1).

Furthermore, the atmospheric forcing used in the ROMS model was sourced from the European Centre for Medium-Range Weather Forecasts Reanalysis 5 (ERA5; Hersbach et al., 2020). To enable atmospheric and oceanic exchange in ROMS, the #define BULK_FLUXES module was activated by referring to Fairall et al. (1996b) to generate 'Upward longwave radiation flux' and 'Downward longwave radiation flux'. In addition, #define LONGWAVE OUT was enabled to directly calculate the net longwave radiation based on the SST model from ROMS. To closely simulate ocean reality, wave coupling to the SWAN model is also applied in this study.

The coupling model of ROMS and SWAN produces the variables R_{sw}, R_{lw}, R_{shf}, and R_{lhf}, U_{10}, and T_b. These six variables are used as ΔT_c and ΔT_w modeling to estimate the T_s.

In the ROMS model, the net sea surface heat fluxes (Q_{net}; W m^{-2}) is the sum of the components:

$$Q_{net} = R_{sw} + R_{lw} + R_{shf} + R_{lhf} \quad (2)$$

Meanwhile, the sea surface cooling flux (Q; W m^{-2}) by ignoring R_{sw} proposed by Fairall et al. (1996a) as:

$$Q = R_{lw} + R_{shf} + R_{lhf} \quad (3)$$

where a Q positive (negative) value means the ocean is warming (cooling). The ROMS model calculates Q_{net} and Q as the difference between the flux downward and the flux emitted.

2.3 Modeling of ΔT_c and ΔT_w

The ΔT_c of this study refers to the experiments of Saunders (1967b), who derived its relationship to seawater viscosity (ν; $m^2\ s^{-1}$), radiation (q; $W\ m^{-2}$) and wind stress (τ; $N\ m^{-2}$) as follows:

$$\Delta T_c = \frac{\lambda q \nu}{k\left(\frac{\tau}{\rho}\right)^{\frac{1}{2}}} \tag{4}$$

where λ is Saunders constant, ρ is the density of the seawater ($kg\ m^{-3}$) and k is the thermal conductivity of the seawater ($W\ m^{-1}\ K^{-1}$). However, this equation is less suitable when used in conditions of weak wind; note that as $\tau \to\sim 0$ then $\Delta T \to\sim$. To overcome this, Fairall et al. (1996a) tried to include shortwave radiation, which would reduce the cooling rate of Eq. (2) as a result, Eq. (4) is rewritten as:

$$\Delta T_c = \frac{\lambda (Q + R_{sw} f_s)\nu}{k u_*} \tag{5}$$

with:

$$\lambda = 6\left[1 + \left(\frac{16 Q_b g \alpha \rho c_p \nu^3}{u_*^4 \times k^2}\right)^{\frac{3}{4}}\right]^{-\frac{1}{3}} \tag{6}$$

$$f_s = 0.137 + 11d - \frac{6.6\times 10^{-5}}{d} \times\left(1 - \exp\left(-\frac{d}{8}\times 10^{-4}\right)\right) \tag{7}$$

$$d = \frac{\lambda \nu}{\left(\frac{\rho_a}{\rho}\right)^{\frac{1}{2}} u_*} \tag{8}$$

and

$$Q_b = Q + \left(\frac{s\beta c_p}{\alpha L_e}\right) R_{lhf} \tag{9}$$

where f_s is the fractional R_{sw} entering the water body; d is the cool skin depth (m); u_* is the wind friction velocity at sea ($m\ s^{-1}$) obtained from the relationship $\sqrt{\tau_a/\rho}$, with $\tau_a = C_a \times \rho_a \times U_{10}^2$ where C_a is the wind friction coefficient over the water surface and ρ_a is the density of air ($kg\ m^{-3}$); Q_b is the salinity buoyancy force due to evaporation ($W\ m^{-2}$); g is the Earth gravity ($m\ s^{-2}$); α is the thermal expansion coefficient of seawater (K^{-1}); c_p is the specific heat of seawater ($J\ kg^{-1}\ K^{-1}$); S is the salinity of the ocean; β is the expansion coefficient of salinity ($kg\ g^{-1}$); and L_e is the latent heat of vaporization ($W\ m^{-2}$).

In addition, the warming effect of the sun during the day, which creates a ΔT_w is also considered. The ΔT_w equation used refers to Zeng and Beljaars (2005) hereafter ZB05:

$$\frac{\partial \Delta T_w}{\partial t} = \frac{Q + R_{sw} - R(-d)}{d\rho c_p \gamma(\gamma+1)} - \frac{(\gamma+1)\kappa u_* \Delta T_w}{d\phi_t\left(\frac{d}{L}\right)} \tag{10}$$

with:

$$\frac{R(-d)}{R_{sw}} = 0.28e^{-71.5d} + 0.27e^{-2.8d} + 0.45e^{-0.07d} \tag{11}$$

$$\phi_t\left(\frac{d}{L}\right) = \begin{cases} 1 + 5d/L & \text{for} \quad d/L \geq 0 \\ (1 - 16d/L)^{-0.5} & \text{for} \quad d/L < 0 \end{cases} \tag{12}$$

where $\kappa = 0.4$ is the von Kármán constant. ZB05 suggested that the warm layer depth, $d = 2 \sim 4$ m may be appropriate where the diurnal fluctuation of ocean temperature is minimal. For $d = 3$ m, ZB05 suggested that $\gamma = 0.3$. Eq. (10) is worked out implicitly using Newton-Raphson method. The above two temperature values when combined with T_b (this study takes at a depth of 10 m from the sea surface) following Ward (2006):

$$T_s = \Delta T_c + T_w + T_b \tag{13}$$

Eq. (13) can be used to calculate the combination of ΔT_c and ΔT_{cw}:

$$\Delta T_{cw} = \Delta T_c + \Delta T_w = T_s - T_b \tag{14}$$

To obtain an easily applicable ΔT_c, Donlon et al. (2002, hereafter D02) constructed the relationship of ΔT_c to U_{10} as follows:

$$\text{D02}\ \Delta T_c = -0.14 - 0.3 \times \exp(-0.27 U_{10}) \tag{15}$$

Equation (13) produces ΔT_c models from other authors, such as Minnett et al. (2011, hereafter M11), Alappattu et al. (2017, hereafter A17), Zhang et al. (2020 hereafter Z20), Luo et al. (2022, hereafter L22), and Yang et al. (2023, hereafter Y23):

$$\text{M11}\ \Delta T_c = -0.14 - 0.3 \times \exp(-0.27 U_{10}) \tag{16}$$

$$\text{A17}\ \Delta T_c = -0.13 - 0.724 \times \exp(-0.35 U_{10}) \tag{17}$$

$$\text{Z20 } \Delta T_c = -0.15 - 0.33 \times \exp(-0.23 U_{10}) \quad (18)$$

$$\text{L22 } \Delta T_{cw} = -0.175 - 0.363 \times \exp(-0.384 U_{10}) \quad (19)$$

$$\text{Y23 } \Delta T_c = -0.169 - 0.411 \times \exp(-0.419 U_{10}) \quad (20)$$

Note that to avoid the influence of R_{shf}, the model data of U_{10} in Equations (15)–(18) and (20) were only made at nighttime. However, in this study, considering the presence of a ΔT_w that acts as a sea surface energy balance, a daytime scenario with a ΔT_w is also considered. As a novelty, this study also offers a new empirical ΔT_c scheme applicable to the Sunda Strait.

2.4 Correction of ΔT_c and ΔT_w

As explained earlier, the ΔT_c and ΔT_w affect the T_b, where the T_b will differ in value from the T_s. Referring to Alappattu et al. (2017), to obtain a T_b value close to the T_s, corrections to the wind speed (ΔT_{cww}) and diurnal cycle (ΔT_{cwd}) are required:

$$\Delta T_{cww} = T_s - T_{bw} \quad (21)$$

$$\Delta T_{cwd} = T_s - T_{bwd} \quad (22)$$

where T_b to wind (T_{bw}) and T_b to wind and diurnal (T_{bwd}) are expressed as:

$$T_{bw} = T_b - \Delta T_{corr_w} \quad (23)$$

$$T_{bwd} = T_{bw} - \Delta T_{corr_d} \quad (24)$$

with ΔT_{cww} correction to U_{10} (ΔT_{corr_w}) and ΔT_{cwd} correction to diurnal (ΔT_{corr_d}) obtained through the least square fit method. Equatrions (23)–(24) are then compared against the T_s to determine the performance of the differences along the correction.

2.5 Statistics analysis

We used the daily Optimum Interpolation Sea Surface Temperature (OISST) Version 2.1 (Huang et al., 2021) as the primary dataset to validate the T_b. OISST is a high-resolution (0.25° × 0.25°) daily blended analysis that combines satellite observations primarily from the Advanced Very High-Resolution Radiometer (AVHRR) with extensive in situ measurements from ships, buoys, and Argo floats. Argo data from above 5 m depth have been incorporated since January 2016. A key feature of OISST is its systematic bias correction of the satellite data against the in situ measurements. This process adjusts the final output to represent the SST at a nominal depth of 0.2 m, which aligns with the definition of T_b. Conversely, to validate the T_s, we employed the AVHRR Pathfinder Version 5.3 (PFV53) Level 3 Collated (L3C) product as an independent satellite source (Casey et al., 2010; Saha et al., 2025). This sensor, aboard NOAA Polar Operational Environmental Satellites (POES) from NOAA-7 to NOAA-19, uses infrared radiometry to retrieve SST from the top millimeter of the ocean surface, representing the physical T_s. Since we use a sigma vertical coordinate system with 50 levels, T_b is extracted at the depth of the last sigma layer (s_rho = 50).

To assess the capability of the model performance (m_i) against the observations (o_i), statistical analyses were conducted including bias, Sum of Squared Errors (SSE), Root Mean Square Error (RMSE) and correlation (r) following established model evaluation frameworks (Willmott et al., 1985):

$$\text{bias} = \frac{1}{n}\sum_{i=1}^{n}(m_i - o_i) \quad (25)$$

$$\text{SSE} = \sum_{i=1}^{n}(o_i - m_i)^2 \quad (26)$$

$$\text{RMSE} = \sqrt{\frac{\sum_{i=1}^{n}(m_i - o_i)}{n}} \quad (27)$$

$$r = \frac{\sum_{i=1}^{n}(o_i - \bar{o})(m_i - \bar{m})}{\sqrt{\sum_{i=1}^{n}(o_i - \bar{o})^2 \sum_{i=10}^{n}(m_i - \bar{m})^2}} \quad (28)$$

Bias, RMSE, and r are used as assessments of m_i (o_i) on ΔT_c (U_{10}), T_b in Eqs. (23)–(24), and U_{10} (T_{cw}). SSE is used specifically to see the difference of U_{10} against the empirical equation resulting from the relationship of U_{10} to ΔT_c. In addition, for validation purposes, the above four assessments were used to compare the T_b generated by the coupled model against the OISST. The smaller the bias, RMSE, and SSE, the better the model performance, while the larger the r, the stronger the agreement.

3. Results

3.1 Variability ΔT_c and ΔT_w

Validation of the modeled T_s against an independent satellite product is crucial for ensuring the reliability of subsequent analyses. Figure 2a shows the comparison between the T_s and satellite-derived T_s from the AVHRR. The statistical assessment comprises bias, SSE, RMSE, and r values

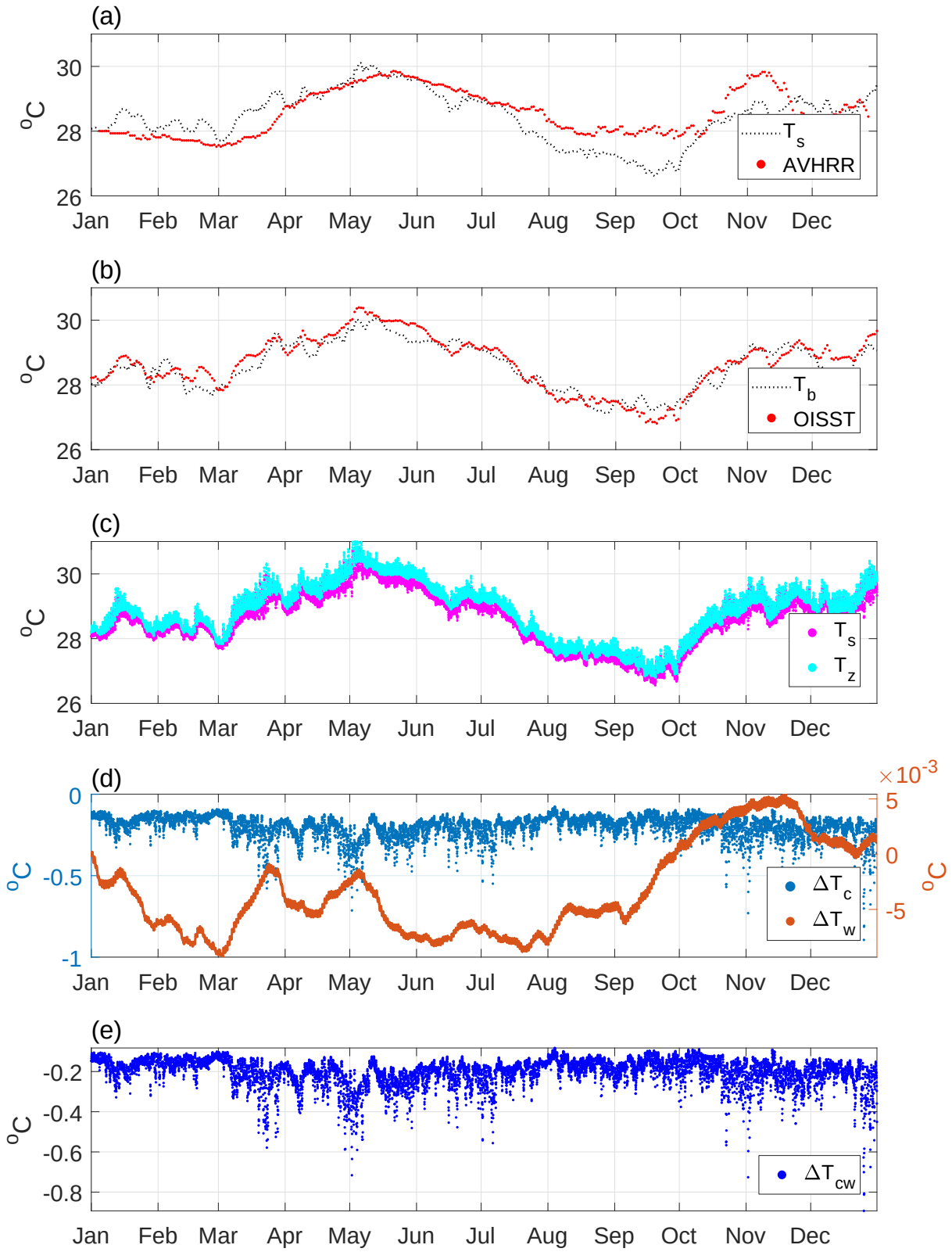

Figure 2. a) Validation of T_s (black dot) coupled model with the AVHRR (red dot). b) Validation of T_b (black dot) coupled model with the OISST (red dot). c) Daily time series of T_s (magenta dot) and T_b (cyan dot). d) Hourly timeseries of ΔT_c (blue dot) and ΔT_w (brown dot). e) Hourly timeseries ΔT_{cw} as the sum of $\Delta T_c + \Delta T_w$. All timeseries in the period 2023.

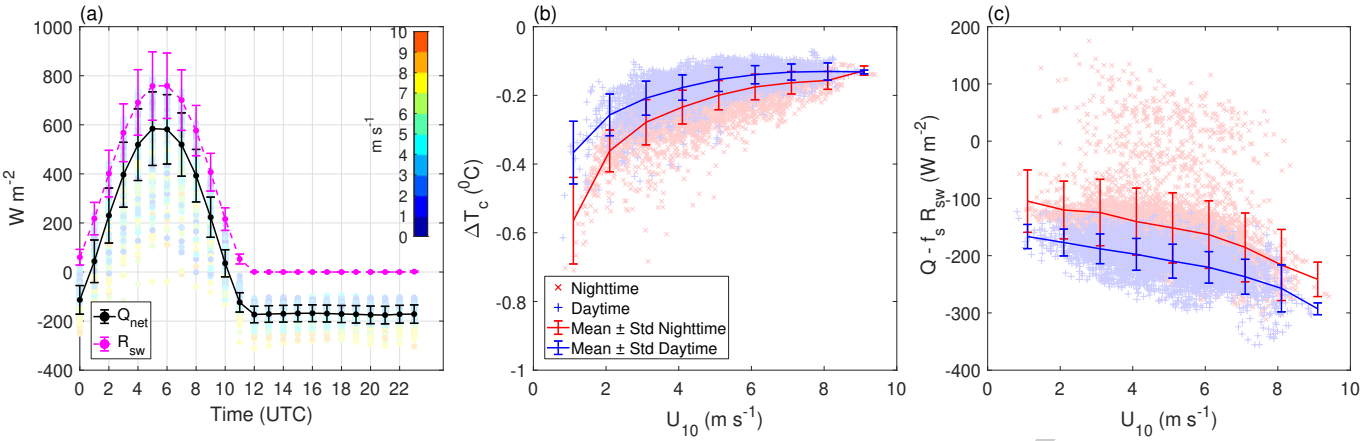

Figure 3. Average diurnal cycle Q_{net} and R_{sw} Sunda Strait Period 2023 with colors representing U_{10} (a), ΔT_{c} (b) and $Q - f_s R_{\text{sw}}$ (c) response to U_{10} nighttime (cross sign) and daytime (plus sign) with 1× standard deviation bar. Local Time (LT) is UTC+7.

of 0.13°C, 113.85, 0.57°C, and 0.71, respectively. Meanwhile, Figure 2b presents the validation of the modeled T_{b} against the OISST product, yielding bias, SSE, RMSE, and r values of 0.12°C, 29.02, 0.28°C, and 0.87, respectively. The significant correlation for the more dynamic T_{s} and the strong statistical agreement for T_{b} provide confidence in the coupled model's performance, justifying its use for subsequent analysis of the cool skin and warm layer effects.

The calculation based on Eq. (13) gives a value of T_{s} following the pattern of T_{b}, where T_{s} is lower than T_{b} (Figure 2b). The two components have a similar pattern to the OISST output. To show the effect of ΔT_{c} and ΔT_{w} corrections on the T_{s} and its comparison to the T_{b} is presented in Figure 2c. At a certain time ΔT_c can reach -0.8°C at the end of December 2023. The ΔT_{w} fluctuates throughout the season, for example, it reaches maximum values in early January, April, May, and reaches a maximum in November. The value of ΔT_{w} is relatively small compared to ΔT_c, which is in the scale of 10^{-3}. In addition, the ΔT_{c} depth based on Eq. (8) is 55 μm with an average ΔT_{c} of -0.2°C throughout the day of the observation period. The difference between ΔT_{c} and ΔT_{cw} within Eq. (14) is presented in Figure 2d. There is no significant difference in the effect of ΔT_{w} in influencing ΔT_{c}. The ΔT_{cw} is still at a negative value throughout the period.

3.2 Wind driven modulation of the ΔT_{c}

As a further analysis to distinguish the diurnal cycle influence, the daytime and nighttime in Figure 3a were determined. Daytime is shown with a quadratic shortwave trend at 07.00–19.00 Local Time (LT), and nighttime is shown with a linear shortwave trend at 19.00–07.00 LT. In addition, it appears that the wind speed generally corresponds to R_{sw} and Q_{net}. This corresponds to low (high) air temperature resulting in high (low) air pressure created from low (high) R_{sw}, which in turn creates high (low) U_{10}. Diurnal heating is frequently correlated with the wind speed. The diurnal heating decreases with increasing wind speed and intensifies with increased insolation. Alterations in wind speed can rapidly influence the magnitude of diurnal heating, whereas changes in insolation have a more gradual effect. These temporal regimes form the basis for analyzing the diurnal characteristics of ΔT_{c} and ΔT_{cw}. Gentemann and Minnett (2008) explained that the timing of the peak diurnal heating can be directly related to the minimum wind speed and varies locally. This finding underscores that diurnal heating is decoupled from insolation periodicity and instead exhibits regional variability governed by wind dynamics. Furthermore, a study conducted by Donlon et al. (2002) provided an estimate of ΔT_{c} with T_{b} influenced by U_{10}, where higher wind speed reduces the ΔT_{c} layer thickness and diminishes the thermal gradient between T_{s} and sub-surface temperatures.

Figure 3b shows that ΔT_c has an U_{10} relationship, with a lower average ΔT_c at nighttime than daytime. This correlates with low wind speeds and increases with high wind speeds, eventually stabilizing within -0.1°C when wind speeds exceed 8 m s^{-1}. This behavior is due to the increase in nighttime R_{lhf} and R_{shf} associated with the increase in wind speed, which also balances the thinning effect of the conduction layer in the T_{s} making ΔT_c independent of wind speed. At low wind speeds (< 8 m s^{-1}), the R_{lw} dominates sea surface heat flux exchange (Murray et al., 2000). Meanwhile, the thinning of the conduction layer that occurs as the wind speed increases is thought to be an increase in ΔT_c (Murray et al., 2000).

Furthermore, Figure 3c presents the relationship of the net surface cooling flux after subtracting the shortwave flux absorbed by water ($Q - f_s R_{\text{sw}}$) against U_{10} at nighttime and daytime. In general, the value of $Q - f R_{\text{sw}}$ decreases as the wind speed increases, both during the daytime and nighttime. This indicates that wind speed plays a role in

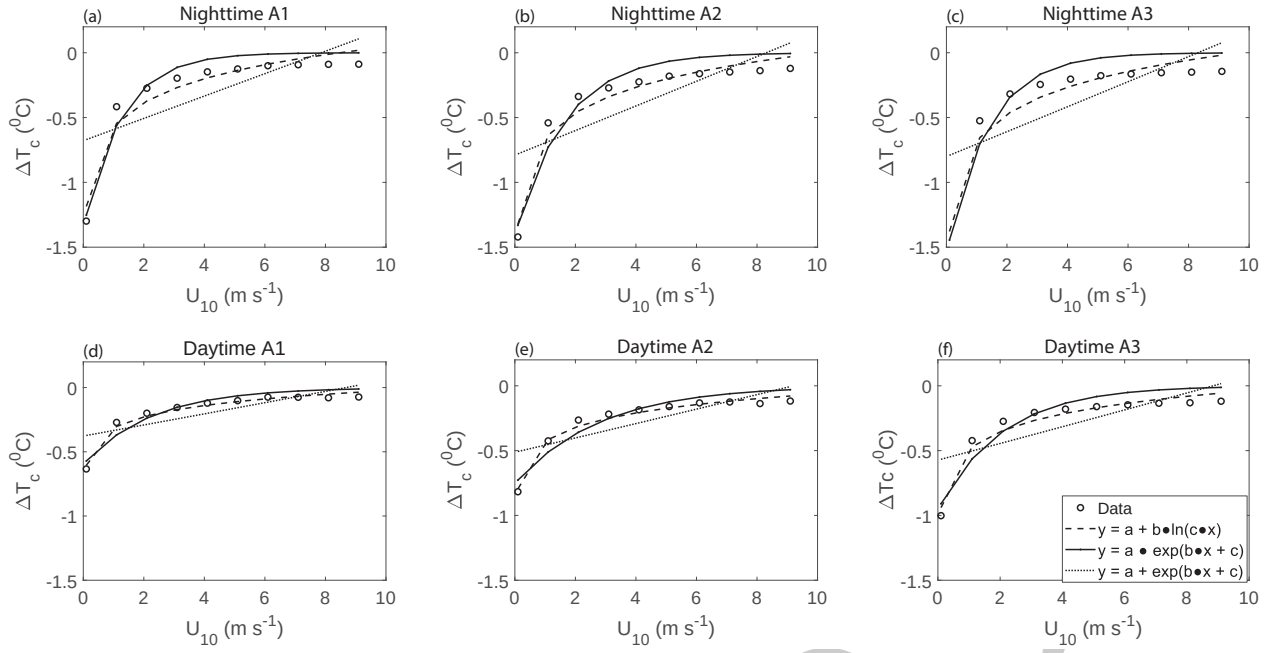

Figure 4. Relationship of ΔT_c as U_{10} at the A1, A2, and A3 sites under nighttime and daytime conditions. The variables a, b, and c in the legend are presented in Table 1.

Table 1. Relationship $\Delta T_c(y)$ as $U_{10}(x)$ at 3 sites during nighttime and daytime, derived from Figure 4 and statistical assessment. Gray shading on the table indicates the highest r.

Site	Diurnal	Model	Bias	RMSE	SSE	r
A1	Nighttime	$y = -0.534 + 0.247 \times \ln(0.975x)$	−0.000	0.044	0.066	0.959
		$y = -0.248 \times e^{-0.709x-1.601}$	−0.049	0.070	0.084	0.934
		$y = -28.457 + e^{-0.003x+3.326}$	−0.002	0.498	0.223	0.527
	Daytime	$y = -0.367 + 0.156 \times \ln(0.984x)$	0.000	0.013	0.036	0.970
		$y = -0.153 \times e^{-0.540x-1.599}$	−0.030	0.042	0.065	0.899
		$y = -21.120 + e^{0.003x+3.030}$	0.001	0.185	0.136	0.558
A2	Nighttime	$y = -0.661 + 0.293 \times \ln(0.971x)$	−0.000	0.056	0.075	0.962
		$y = -0.294 \times e^{-0.625x-1.595}$	−0.062	0.135	0.116	0.908
		$y = -36.040 + e^{-0.003x+3.562}$	−0.002	0.679	0.261	0.540
	Daytime	$y = -0.461 + 0.174 \times \ln(0.982)$	0.000	0.010	0.032	0.980
		$y = -0.169 \times e^{-0.369x-1.588}$	−0.025	0.061	0.078	0.881
		$y = -18.042 + e^{-0.003x+2.862}$	0.002	0.203	0.142	0.603
A3	Nighttime	$y = -0.683 + 0.307 \times \ln(0.969x)$	0.000	0.107	0.104	0.936
		$y = -0.321 \times e^{-0.746-1.601}$	−0.082	0.167	0.129	0.900
		$y = -47.603 + e^{-0.002x+3.846}$	−0.001	0.869	0.295	0.479
	Daytime	$y = -0.540 + 0.228 \times \ln(0.976)$	0.000	0.041	0.064	0.954
		$y = -0.230 \times e^{-0.568-1.593}$	−0.054	0.109	0.104	0.879
		$y = -22.664 + e^{-0.003x+3.092}$	0.002	0.432	0.208	0.518

the process of reducing heat from the ocean through R_{shf} and R_{lhf}. It can be seen that the value is consistently higher at nighttime than during the daytime at the same wind speed. This difference is due to the contribution of R_{sw}, which is present only during the daytime, reducing the efficiency of the Q. In contrast, nighttime heat loss occurs exclusively through the upward fluxes of R_{lw}, R_{shf}, and R_{lhf} in the absence of R_{sw}. Consequently, the increase in wind at nighttime, which is not offset by R_{sw}, causes a higher $Q - fR_{\text{sw}}$.

The Sunda Strait has three distinct water characteristics such as A1, A2, and A3, as shown in Figure 1. To determine the best empirical link between U_{10} and ΔT_c diurnally, we compared numerous equations using curve

fitting (Figure 4). Both at nighttime and daytime, ΔT_c follows a similar pattern in the three sites. At nighttime, ΔT_c is lower at wind speed (~ 0.1 m s^{-1}) than during the daytime. The ΔT_c value expands up to 4 m s^{-1} and remains constant after that. The best relationship between U_{10} and ΔT_c can be expressed as $y = a + b \times \ln(c \times x)$. The logarithmic equation appears to satisfy the equation of U_{10} compared to ΔT_c based on the obtained correlation (> 0.9). In more detail, this equation performs well during the daytime (Table 1).

3.3 Correction scheme for T_s retrieval

In this study, we refine the skin-bulk temperature difference by considering the contribution of shortwave radiation to ΔT_w formation. In contrast to previous studies that focused on the influence of wind speed (Donlon et al., 2002) or omitted daytime radiative heating processes (Minnett, 2003; Ward, 2006), we introduce a corrected skin-bulk temperature difference defined in Eq. (14) in the form of ΔT_{cw}. This correction is based on the mechanistic that solar radiation significantly alters the vertical temperature profile near-sea surface, particularly under low-wind regimes where turbulent mixing is suppressed (Fairall et al., 1996a). Including ΔT_w results in a more realistic representation of the thermal conditions near the sea surface.

Two steps of ΔT_{cw} correction were applied sequentially based on U_{10} and diurnal cycle. The least-squares fit method was used for the correction. It can be seen that the correction of ΔT_{cw} to U_{10} has an increasing exponential trend and the correction to diurnal has a sinusiodal pattern. Specifically, the fitting of the correction of ΔT_{cw} to U_{10} and diurnal (t), respectively, is given as:

$$\Delta T_{\mathrm{corr_w}} = -0.149 - 0.613 \times e^{-0.548 \times U_{10}} \quad (29)$$

$$\Delta T_{\mathrm{corr_d}} = -0.41 + 0.03 \times \sin(0.25t + 0.13) \quad (30)$$

To calculate the correction for ΔT_{cww} and ΔT_{cwd} by using Eqs. (21)–(22), the T_b is derived from Eqs. (23)–(24)

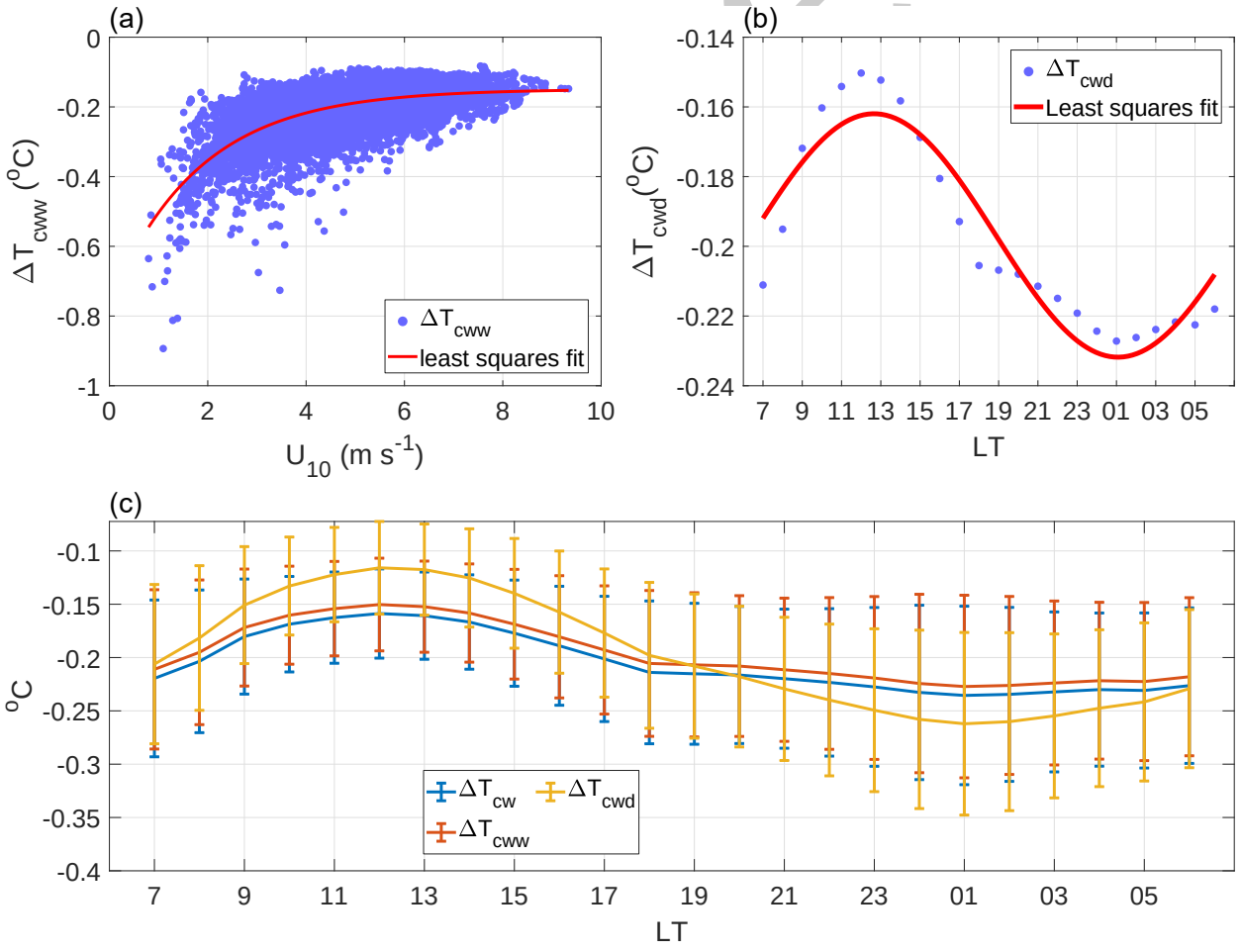

Figure 5. Correction of T_{cw} to U_{10} (a), T_{cw} to diurnal (b), and hourly variability of ΔT_{cw}, ΔT_{cww}, and ΔT_{cwd} with 1× standard deviation expressed by bars (d). Local Time (LT) is UTC+7.

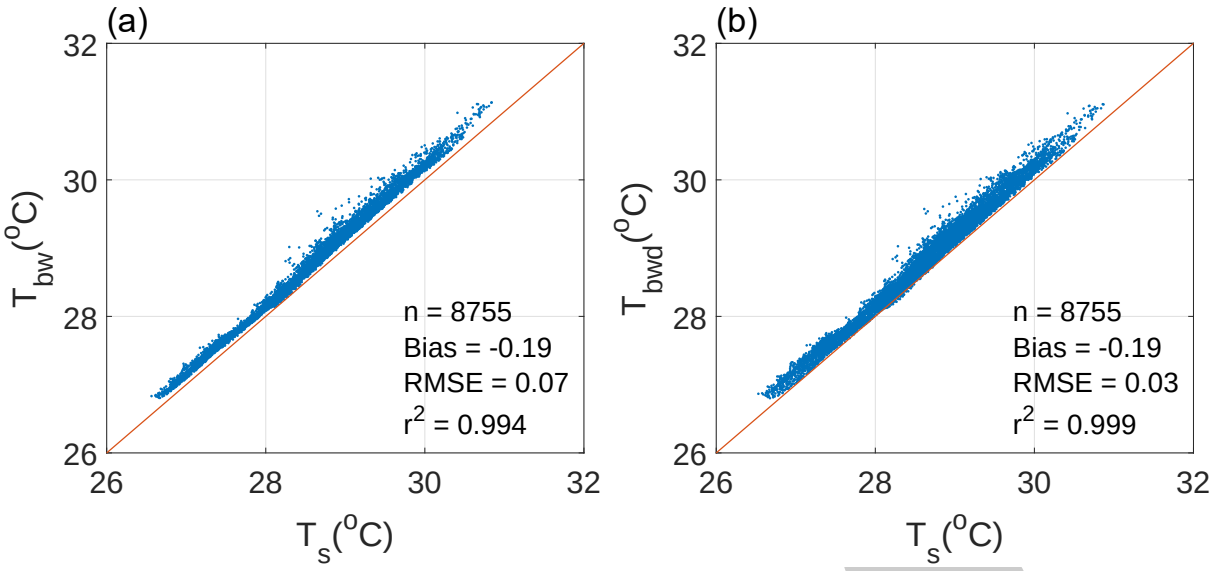

Figure 6. Scatterplot of the relationship between T_s and T_b after correction for U_{10} (a) and diurnal variability (b). The brown line represents 1:1.

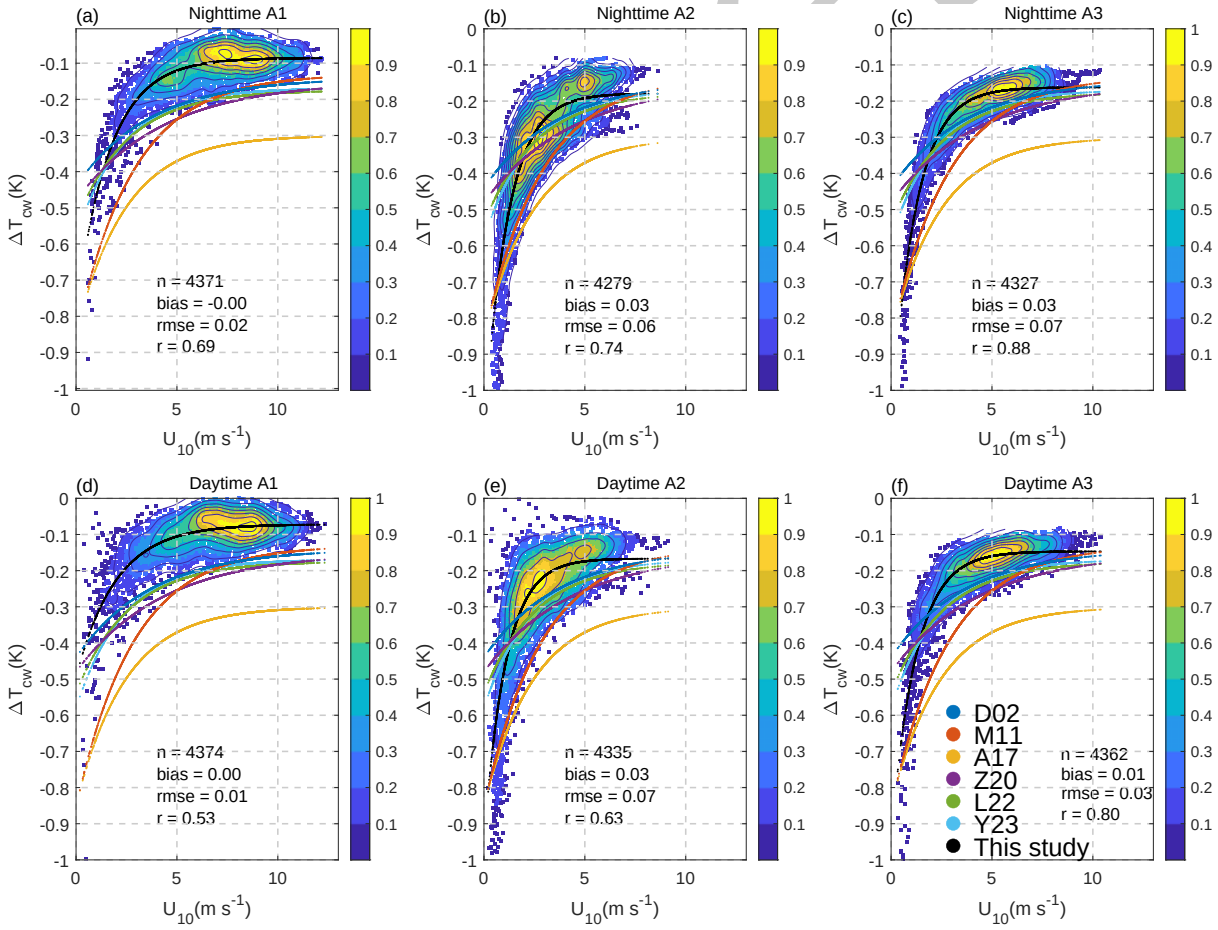

Figure 7. Exponential plot of ΔT_{cw} against U_{10} between the models at the 3 sites at nighttime and daytime. The colorbar and contour lines represent the percentage data density and data density interval of 10%, respectively.

Table 2. Exponential function of ΔT_{cw} to U_{10} nighttime and daytime in the Sunda Strait.

Site	Nighttime	Daytime
A1	$\Delta T_{cw} = -0.086 - 0.696 \times e^{-0.599 \times U_{10}}$	$\Delta T_{cw} = -0.072 - 0.423 \times e^{-0.507 \times U_{10}}$
A2	$\Delta T_{cw} = -0.179 - 0.942 \times e^{-0.855 \times U_{10}}$	$\Delta T_{cw} = -0.167 - 0.783 \times e^{-0.926 \times U_{10}}$
A3	$\Delta T_{cw} = -0.162 - 0.930 \times e^{-0.833 \times U_{10}}$	$\Delta T_{cw} = -0.147 - 0.795 \times e^{-0.819 \times U_{10}}$

by using Eqs. (29)–(30). Figure 5a–c reveal a negative ΔT_c, which contributes to an overall ΔT_w in the studied region. This observation implies an efficient transfer of heat flux from the ocean to the atmosphere. This result confirms that the Sunda Strait does not experience the warm skin effect, which is the opposite effect of ΔT_c, where the SST is warmer than the underlying layer. Warm skin findings are often found in high latitudes where the air is more humid and warmer than the SST and can account for up to 10% of the total observational data (Yang et al., 2023; Zhang et al., 2020).

Furthermore, the diurnal variability of the corrections from Equations (21)–(22) in Figure 5c reveals that all ΔT_{cw} values remain negative throughout the entire period. This indicates that the influence of ΔT_{cw} exerts a minimal effect on the increase of T_s in the Sunda Strait. The uncorrected ΔT_{cw} initially exhibited values of approximately -0.2°C. After applying the wind speed correction, these adjusted values were slightly higher across all time periods. Finally, the diurnal correction yielded higher values during the peak insolation and nighttime periods, specifically around 11.00–13.00 and 23.00–03.00 LT, respectively. All three ΔT_{cw} patterns in Figure 5c display a maximum value at 12 LT, nearly coinciding with the peak insolation.

To derive the true T_s by eliminating the effects of ΔT_c and ΔT_w, the ΔT_{cw} correction from Eqs. (29)–(30) was applied to compute the T_b correction based on Eqs. (23)–(24), as illustrated in Figure 6. The bias was uniform with a progressively decreasing RMSE. Furthermore, the two-step correction yielded a near-perfect correlation (Figure 6b) compared to the U_{10} correction (Figure 6a). Both correction methods resulted in a similar overall data distribution, although with greater scatter within the 27–31°C range. All correction treatments resulted in values slightly above the 1:1 line, indicating that the T_b estimates were systematically higher than the T_s. Nevertheless, applying either the U_{10} or diurnal correction successfully removed the influence of ΔT_c and ΔT_w, enabling an accurate estimation of the T_s in the Sunda Strait.

3.4 Modeling performance of ΔT_{cw}

The relationship of U_{10} to ΔT_c corresponds to the logarithmic equation as illustrated in Table 1. The equation omits the ΔT_w correction due to the influence of the shortwave radiation throughout the day, which persists throughout the night. Figure 7 shows a comparison of the ΔT_{cw} model capability assessment against other authors for diurnal conditions at three Sunda Strait Eqs. (15)–(20). In general, the three sites have a ΔT_{cw} range of 0 to -1°C with limited wind speeds of 9 m s^{-1}, 10 m s^{-1} and 12 m s^{-1} at A2, A3, and A1, respectively.

In comparison to the previous models, the new model (solid black line in Figure 7) demonstrates superior consistency in describing the relationship U_{10} and ΔT_{cw}, whereas A17 and M11 yield less satisfactory outcomes in this study domain. The observed water types indicate that A17 and M11 were conducted in coastal waters, specifically in southeastern New Zealand and North Carolina, respectively. In contrast, this study was conducted in open waters. This condition is similar to D02, Z20, L22, and Y23, which each observed T_s in the Pacific and Atlantic Oceans, Antarctica, Florida Waters, and the South China Sea, respectively. Different types of waters can produce different wind conditions and ocean surface boundary layer dynamics. This implies that the empirical equation of ΔT_{cw} will depend on the local water and atmospheric conditions. The model finally performs best at nighttime due to the gradual reduction of the ΔT_w.

The comprehensive empirical correlation of ΔT_{cw} to U_{10} is illustrated in Table 2. At the three sites, it is evident that the results vary depending on the time of day. The exact formula to describe this relationship can be written as an exponential equation, $\Delta T_{cw} = a + b \times e^{c \times U_{10}}$. This result is different from the condition when considering ΔT_c in Table 1, which gives a logarithmic relationship. It is found that the values of variables a, b, and c during the daytime are larger than those at nighttime (take note the minus sign). This shows the influence of the ΔT_w effect of the shortwave radiation penetrating the water surface. Specifically, A2 gives higher variable values than other locations due to low wind speed due to consequence of narrow waters (i.e., strait). In contrast, A1, which represents the open ocean, gives lower variable values due to the wind influence from the open ocean. Nevertheless, the best correlation is given by A3, which represents enclosed water (Java Sea) up to 0.88. This indicates that wave interaction can retain heat at the water surface more effectively in enclosed waters than in the open ocean, where strong winds lead to significant mixing of the cooler surface and warmer layers.

3.5 Are T_s and ΔT_w influenced by the SWH or current speed?

Figure 8a–c illustrates the relationship between SWH and T_s in the study area. The SWH frequency distribution exhibited distinct characteristics in each area. In the A1, SWH

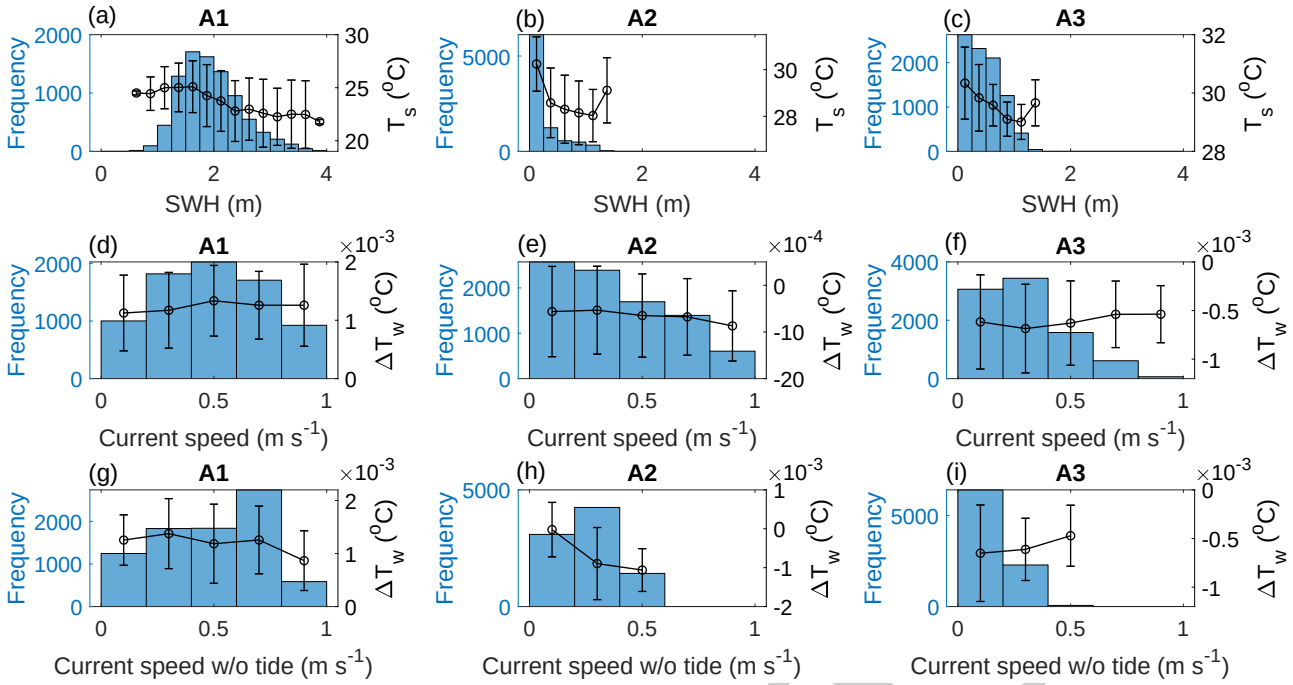

Figure 8. Dependency of T_s on the SWH (a–c), ΔT_w on the current speed (d–f), and ΔT_w current speed without the tide effect (g–i) at the A1, A2, and A3 sites.

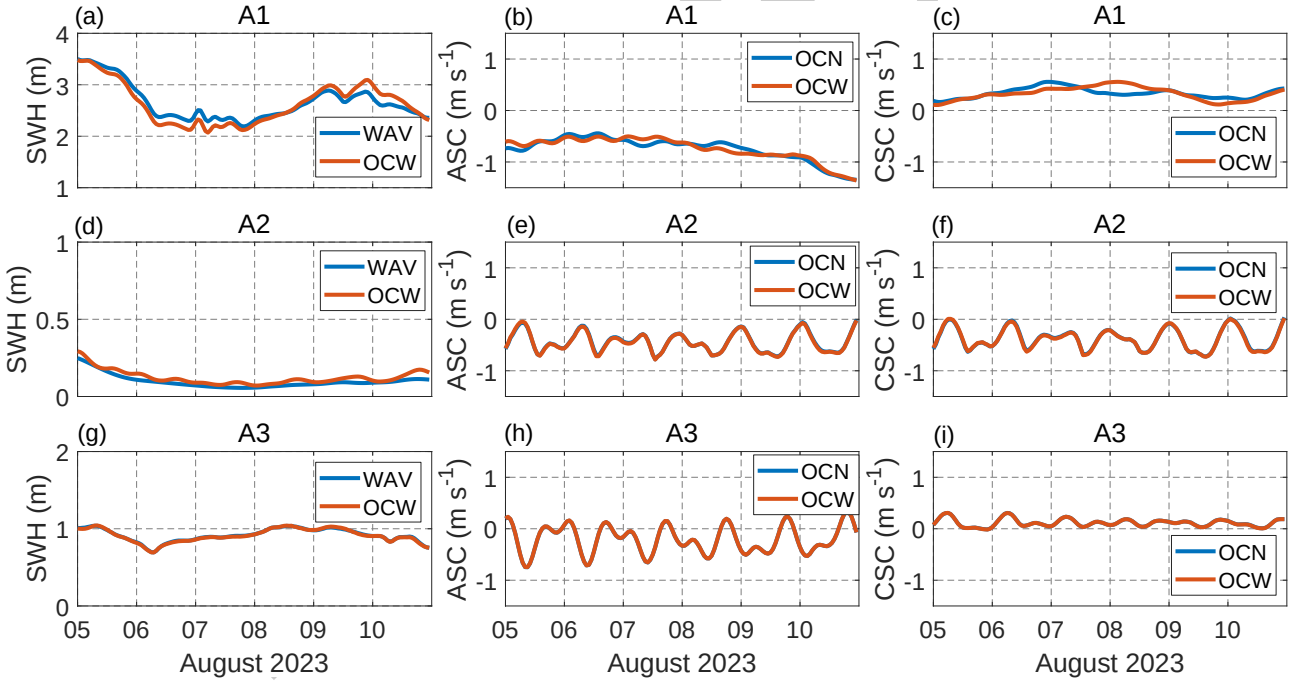

Figure 9. Time series of the SWH, Along-Strait Current (ASC) and Cross-Strait Current (CSC) at the A1, A2 and A3 sites on 5–10 August 2023. The blue line represents a single scenario (WAV for SWAN and OCN for ROMS), while the brown line corresponds to a couple of scenarios (ROMS and SWAN).

ranges more widely (up to ~ 4 m) with a mode around 2 m, indicating the dominance of energetic open-ocean conditions. The relationship between T_s and SWH shows a trend of decreasing T_s with increasing wave height, suggesting enhanced turbulent processes and vertical mixing within the water column. Conversely, in sites A2 and A3 the SWH range is narrower (< 2 m) and T_s tends to be lower, reflecting the influence of the semi-enclosed waters and the

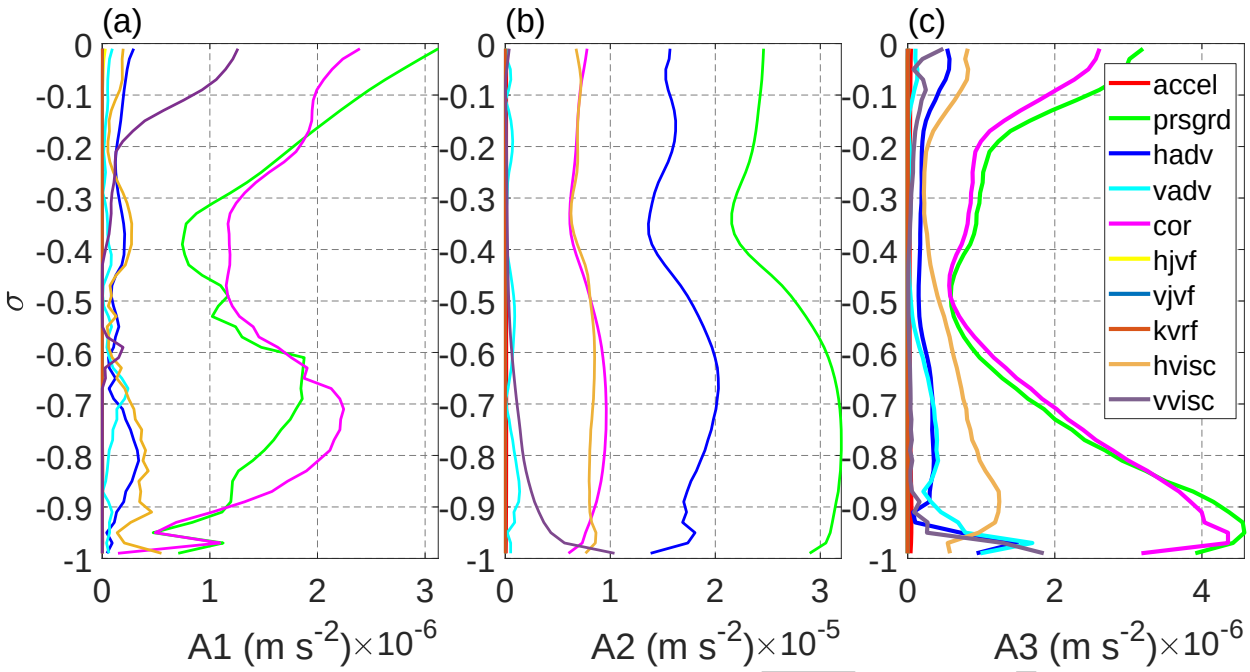

Figure 10. Resultant momentum profile at the A1, A2, and A3 sites. *Accel*: acceleration; *prsgrd*: pressure gradient; *hadv*: horizontal advection; *vadv*: vertical advection; *cor*: corriolis; *hjvf*, *vjvf*: horizontal vortex force; *kvrf*: vertical vortex force; *hvisc*: horizontal viscosity, and *vvisc*: vertical viscosity.

lower wave energy. Analysis of these three sites indicates that SWH corresponds to T_s. Figure 8d–f shows the relationship between the total current speed and ΔT_w at study area. In site A1, although ΔT_w is on the order of 10^{-3}°C, it increases with the current speed, despite high variability. In site A2, ΔT_w decreases weakly with decreasing current speed, whereas in site A3, ΔT_w increases with decreasing current speed.

The Sunda Strait is known for its strong tidal currents (Putri, 2005), which cause intense turbulent vertical mixing, thereby disrupting diurnal stratification and preventing the formation and maintenance of a near-surface warm layer. Therefore, we decomposed the current components by removing the residual current and applied a 30-day Low-Pass Filter (LPF) at the three sites (Pawlowicz et al., 2002). The residual current was used to remove the tidal component, while the LPF was applied to isolate variability shorter than 30 days (intraseasonal). Subsequently, we removed the tidal component and applied the LPF to examine the relationship between the current speed and ΔT_w (Figure 8g–i). The current speed in this scenario is relatively low compared to Figure 8d–f due to the removal of tidal components. The variation of ΔT_w with current speed is consistent in the Indian Ocean and the Sunda Strait, but not in the Java Sea (Figure 8d–i). We hypothesize that this is influenced by wave effects, based on the fact that the Indian Ocean is an open ocean with higher waves compared to the Sunda Strait and the Java Sea. Consequently, further analysis was conducted by comparing the interactions of currents without and with waves (Figure 9).

Figure 9a–i presents the time series of SWH, ASC, and CSC at three sites. Site A1, characterized by higher SWH than sites A2 and A3, exhibits dynamics where wave-driven processes are highly dominant. As a result, the coupled scenario simulates surface currents that are substantially different from the single scenario. In contrast, at sites A2 and A3, the primary dynamics controlling the currents are dominated by tidal forcing and geostrophic influences (a combination of the pressure gradient and Coriolis effect), resulting in negligible differences between the two scenarios. To reinforce this statement, the momentum profiles at each site were calculated based on Olabarrieta et al. (2011, Equations (1) and (2)), as shown in Figure 10. The analysis reveals a site-dependent dominance of terms: at A1, the pressure gradient and Coriolis terms are dominant, reaching their maximums at the surface (3.12×10^{-6} m s^{-2} and 2.4×10^{-6} m s^{-2} respectively); at A2, the balance shifts to include horizontal advection and the J vortex force, pressure gradient, and Coriolis term peaking sharply at mid-depth ($\sigma = -0.7$); whereas at A3, the pressure gradient and Coriolis terms are again dominant, but with their maximums occurring at the seabed (3.91×10^{-6} m s^{-2} and 3.18×10^{-6} m s^{-2}, respectively).

3.6 Effect of T_s, U_{10}, and the sea surface energy balance on oceanic regimes and seasonality

The impact of ocean regimes and seasonal variations on T_s, U_{10}, and sea surface energy balance components through-

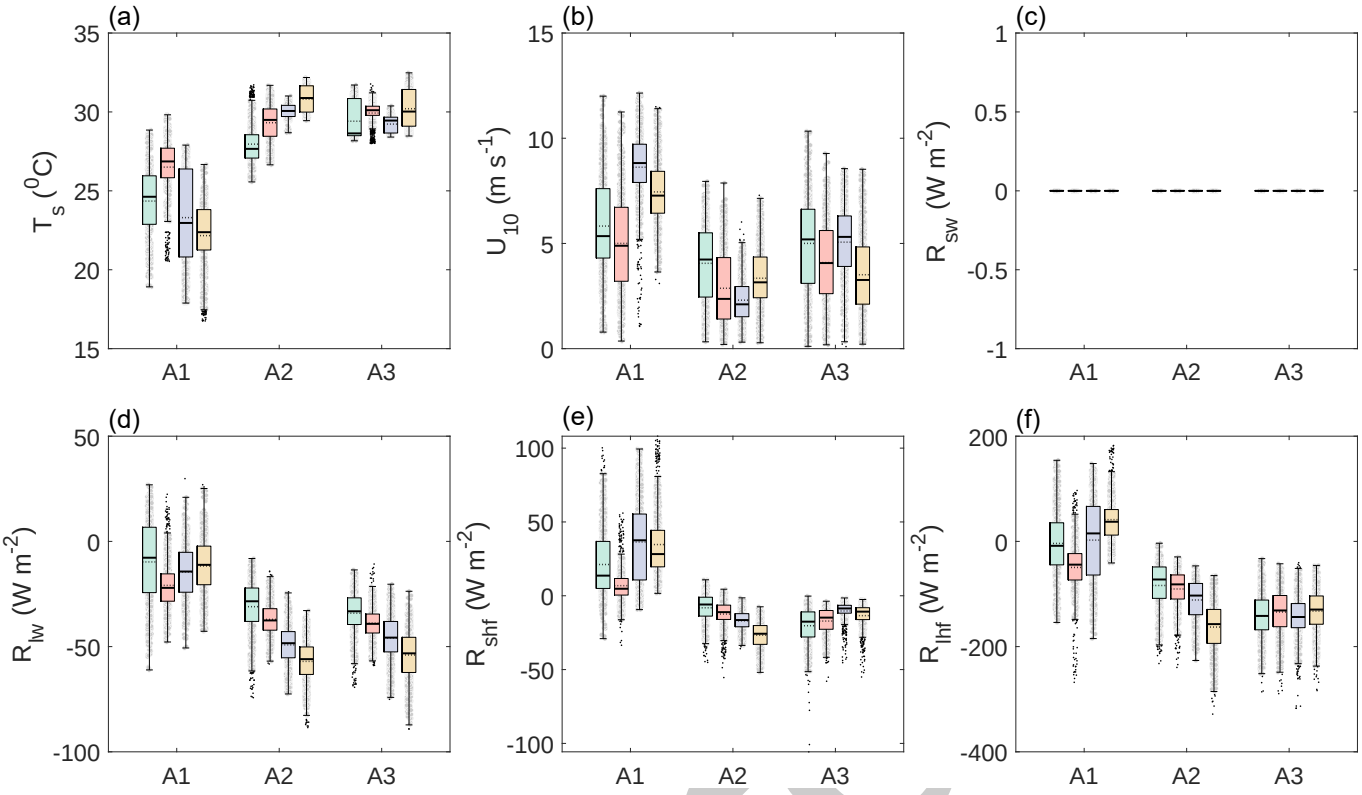

Figure 11. Boxplots of nighttime T_s (a), U_{10} (b), R_{sw} (c), R_{lw} (d), R_{shf} (e), and R_{lhf} (f) at the A1, A2, and A3 sites. The boxplots display the median (solid line within the box), mean (dotted line within the box), observed data (gray dots), and outliers (solid dots). The boxes represent the 25th–75th percentile range, and the whiskers extend to the 5th–95th percentile range.

out both nighttime and daytime is illustrated by the boxplots in Figures 11 and 12, respectively. The T_s distribution at the three sites exhibited significant seasonal fluctuations under both scenarios. At the A1 site, the T_s values tend to be lower than those at A2 and A3, with a temperature increase observed from the DJF to MAM seasons. The temperature in A2 during the DJF season is lower than in other seasons and stays generally stable at 30°C under both nighttime and daytime. This pattern suggests that wide waters, such as the Indian Ocean, affect sea surface cooling more than the relatively confined Sunda Strait and Java Sea. The wind velocity at a height of 10 m (U_{10}) depicted in Figures 11b and 12b, exhibits a seasonal trend. A1 receives relatively increased wind speeds, particularly during the JJA and SON seasons. At the A2 site, U_{10} shows a lower value compared to the other two sites. This relates to the topography of the Sunda Strait, which tends to be narrow. The U_{10} value achieves its minimum during the JJA season and then increases in SON. At the A3 site, the wind speed pattern shows a slight increase relative to A1, but stays below the level of A1. This is due to A3 being open water, as it is part of the Java Sea, which connects to the Pacific Ocean via the South China Sea.

The R_{sw} produces substantial results under both nighttime and daytime scenarios (Figures 11c and 12c). During the nighttime, the R_{sw} is about 0 W m^{-2}. In comparison to daytime, the R_{sw} values were around 400 W m^{-2}. This shortwave flux represents the typical average insolation at the equator. The R_{sw} is relatively uniform across all areas, with an increase during the SON season. Unlike shortwave radiation from the sun, longwave radiation is emitted by the earth's surface and atmosphere. In the oceanography and meteorology context, R_{lw} indicates the energy transmitted from the atmosphere to the ocean. Negative R_{lw} refers to energy transferring from the ocean to the atmosphere. In Figures 11d and 12d, nearly all locations and seasons show negative R_{lw}, except for specific times during the DJF season when A1 is positive. This shows the dominant role of R_{lw} reflected from the ocean to the atmosphere. R_{lw} decreased with increased seasonality at A2 and A3, while remaining stable during the JJA and SON seasons at A1.

The transfer of energy between the ocean and the atmosphere should be analyzed not only through incoming radiation but additionally by considering the energy balance of both the sea surface and the atmosphere. Consequently, the R_{shf} and R_{lhf} energy balances emerge. R_{shf} is the energy exchanged because of the temperature disparity between

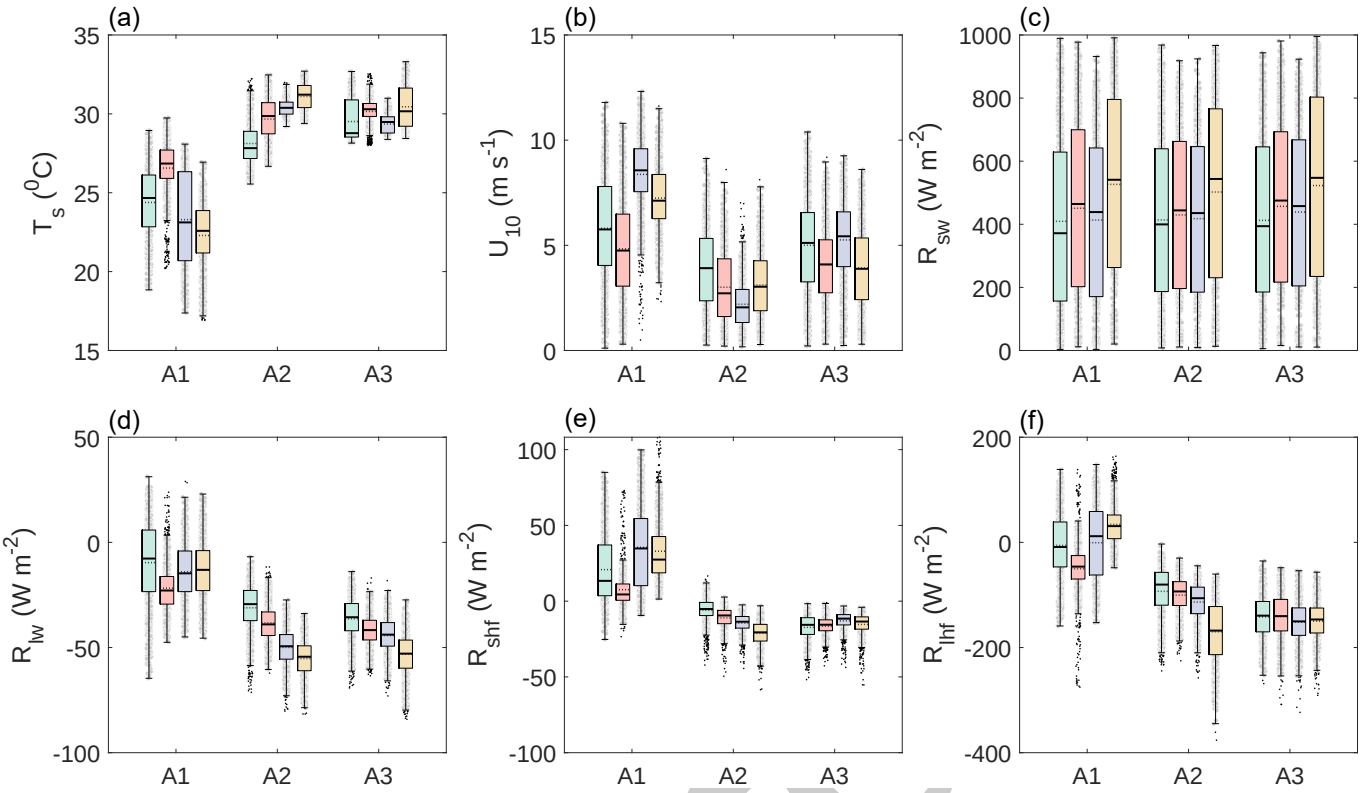

Figure 12. Boxplots of daytime T_s (a), U_{10} (b), R_{sw} (c), R_{lw} (d), R_{shf} (e), and R_{lhf} (f) at the A1, A2, and A3 sites. The boxplots display the median (solid line within the box), mean (dotted line within the box), observed data (gray dots), and outliers (solid dots). The boxes represent the 25th–75th percentile range, and the whiskers extend to the 5th–95th percentile range.

the atmosphere and the ocean. In this study, the sign convention for R_{shf} will be positive if there is a flux from the atmosphere to the ocean, and vice versa. Figures 11e and 12e illustrate that A1 consistently shows positive mean values over all seasons, but A2 and A3 have negative mean values across the same temporal range. This indicates that in the Indian Ocean, the R_{shf} from the atmosphere is more dominant. In the Sunda Strait, the R_{shf} transferring from the ocean to the atmosphere is particularly significant. This phenomenon relates to the linear correlation between wind speed and R_{shf}, where high (low) wind speed causes R_{shf} to increase (decrease) and T_s to decrease (increase).

Furthermore, R_{lhf} refers to the energy used (released) during the phase change of water through evaporation (condensation). This mechanism does not affect a direct change in temperature but rather stores energy. In this study, R_{lhf} is positive when there is an input of energy from the atmosphere to the ocean, and vice versa. Generally, the R_{lhf} in the sea is positive, indicating that energy is leaving the ocean through evaporation. Figures 11f and 12f illustrate that at sites A2 and A3, the entire season is defined by negative R_{lhf}. Some areas of positive R_{lhf} are observed at A1 throughout the season, indicating evaporation activities due to elevated air temperatures relative to the sub-surface water (Pinker et al., 2014).

4. Discussions

This study implemented two sequential corrective procedures, such as the elimination of U_{10} and diurnal cycle effects. The two-step corrections successively produce a T_b that almost resembles T_s, where the combined corrections produce a perfect correlation between T_b and T_s. This indicates that the correction steps can remove the influence of ΔT_c and ΔT_w from the T_b to obtain accurate T_s. This study calculated T_s by including ΔT_c and ΔT_w influences, recognizing that daytime shortwave radiation can extend several hours beyond sunset. This study conforms to Alappattu et al. (2017), who also considered the effects of ΔT_c and ΔT_w.

Furthermore, by considering ΔT_c and ΔT_w effects, it is possible to find the relationship of U_{10} in the Sunda Strait in the diurnal scenario. By comparing with the previous study, the new model can describe the combined relationship of ΔT_c and ΔT_w effects on U_{10} with a correlation range of 0.53–0.88. Here, the Java Sea, as enclosed body of water, provides a better correlation than the open ocean. This is due to the lack of interaction of currents and waves that can mix the surface layer of water, allow-

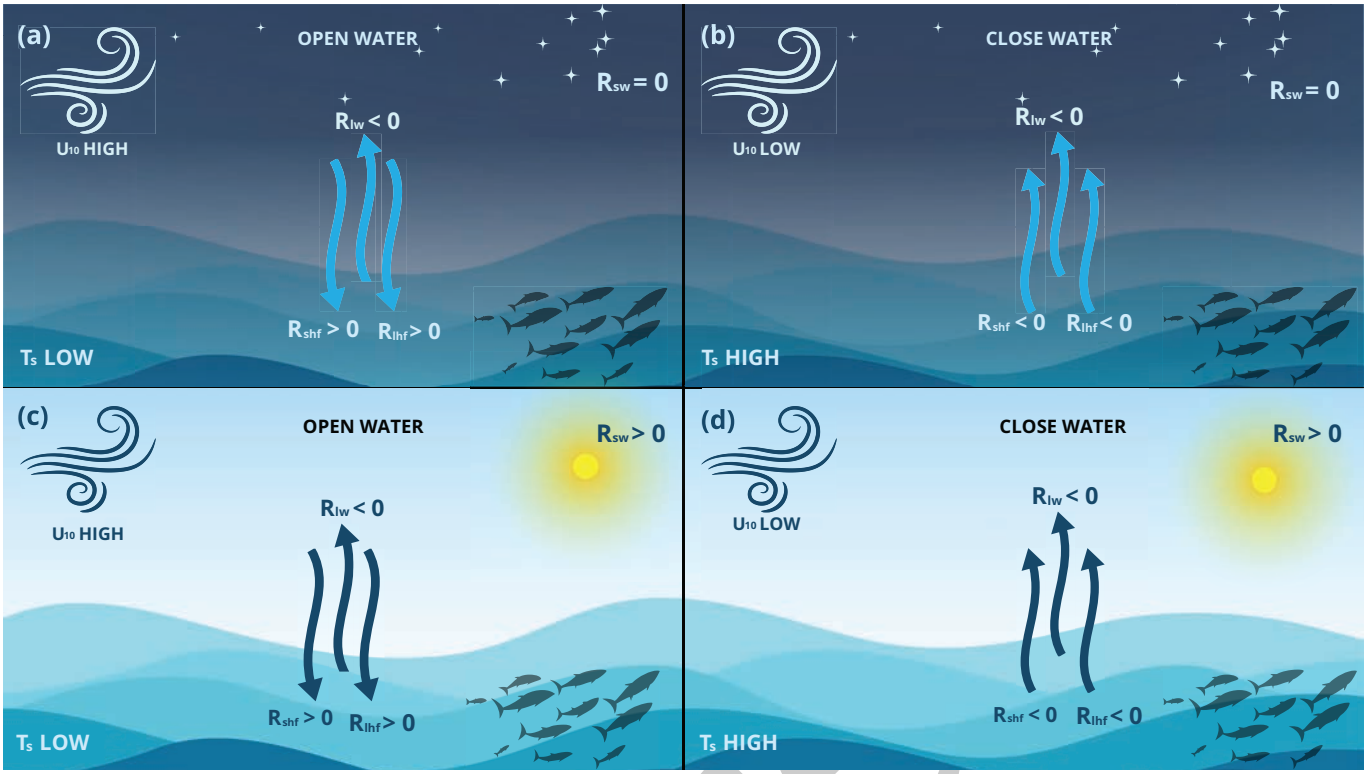

Figure 13. Schematic diagram of T_s, U_{10}, and the sea surface energy balance components (R_{sw}, R_{lw}, R_{shf}, and R_{lhf}) at nighttime and daytime in the open ocean (a,c) and closed waters (b,d).

ing the heat flux to be well retained. Takaya et al., (2010) presented a refinement of the T_s scheme by modifying the Monin-Obukhov similarity function and incorporating the Langmuir circulation effect, resulting in improved accuracy in representing the diurnal SST variability compared to the Zeng and Beljaars (2005) scheme. This indicates the role of the Langmuir circulation in enhancing the mixing and reducing the diurnal variability of the SST in wavy conditions and emphasizes the importance of considering ocean wave effects in modeling. Zhang et al. (2019) also obtained a strong (moderate) dependence between ΔT_c and the wave height (slope), although the dependence on the probability of wave breaking was less pronounced. This has demonstrated the contribution of the wave dynamics to T_s variability.

Furthermore, the critical role of wave dynamics in modulating the T_s and the T_w is evidenced by the contrasting regimes in the Java Sea and the Indian Ocean (Figures 11 and 12). In the wave-dominated Indian Ocean, vigorous wave-driven mixing, which has been shown to correlate with wave height and slope (Zhang et al., 2019), efficiently suppresses diurnal warming by enhancing vertical mixing, thereby reducing T_s variability. Conversely, the Java Sea exhibits an anomalous positive correlation between weak currents and increased ΔT_w, where the lack of strong wave-current interaction minimizes turbulent mixing. This allows for greater heat retention and the development of pronounced diurnal stratification, a regime that our new model captures more effectively due to the dominant control of local heat flux over mixing processes.

The results in Section 3.6 show the temporal variations of the sea surface cooling process associated with oceanographic processes and atmospheric influences. The Indian Ocean has a more effective cooling mechanism compared to semi-enclosed regions such as the Sunda Strait and Java Sea. Upwelling is an ocean phenomenon that results in a lower SST in the open ocean. In the Indian Ocean, particularly south of Java, upwelling is driven by the southeast monsoon winds, which displace surface water, allowing deeper, colder water to ascend (Chakraborty et al., 2023; Putri, 2005). In contrast, enclosed seas such as the Java Sea experience limited water mass exchange. The depth of the Java Sea averages 40 meters and is connected to the Indian Ocean through the Sunda Strait. During the southeast monsoon season, the Java Sea receives colder, higher-salinity water from the Indian Ocean, while during the northwest monsoon season, the Java Sea receives warmer, fresher water from the South China Sea (Siregar et al., 2017; Putri, 2005). These seasonal variations in water mass exchange influence the SST in the Java Sea, which tends to be warmer than the open ocean due to reduced upwelling and higher surface water retention. Then, the monsoon become the dominant atmospheric influence in the Indian Ocean and Java Sea. The southeast monsoon in-

creases upwelling south of Java, resulting in reduced SST in the open ocean (Chakraborty et al., 2023; Putri, 2005). As a result, the T_s decreased during JJA and SON in A1 (Figures 11 and 12). In the Java Sea, the monsoon also affects the SST, but its effect is not dominant due to the shallower bathymetry and limited upwelling (Haryanto et al., 2019; Siregar et al., 2017).

Based on the previous explanation, the SST skin is influenced by oceanic and atmospheric factors, which in turn are related to the components of the diurnal sea surface energy balance. Therefore, in this study, we propose a schematic diagram of the relationship between SST and the diurnal sea surface energy balance in open and enclosed waters (Figure 13). On both nighttime and daytime diurnal scales, wind speed is the dominant meteorological factor affecting R_{shf} and R_{lhf}. In the open ocean, higher wind speeds increase turbulent mixing, leading to increased R_{shf} and R_{lhf} (Fernández et al., 2023; Song, 2023). In contrast, the enclosed ocean experiences decreased wind speed due to coastal orography and land-sea wind interactions, leading to diminished R_{shf} and R_{lhf} (Ganeshan and Wu, 2016; Tomita et al., 2016).

During the daytime, open water experiences a diurnal ΔT_w due to the absorption of solar radiation. This warming is modulated by wind speed, with higher wind speeds reducing the amplitude of the diurnal warming by increasing the turbulent mixing (Yan et al., 2023). Figures 11a,b and Figures 12a,b illustrate the opposite relationship between T_s and U_{10}. This result aligns with those of Hsu (2022) and Yang et al. (2023) that T_s in open water is often slightly cooler than the underlying layer under strong wind conditions. This study also obtained a smaller R_{shf} than R_{lhf} (Figures 11e,f and 12e,f), where the R_{shf} increased under low T_s conditions. Luo et al. (2022) and Yan et al. (2023) also suggested that R_{shf} increases during the cold skin effect period at night, but in this study, it is also seen during the daytime. In open water, R_{lhf} is driven by the moisture gradients and wind speed. When SST is higher, it increases R_{lhf} (Hussein, 2022). However, in this study, high values of R_{lhf} occurred at low T_s (Figure 13a,c). This is probably due to the high wind speed in the open ocean, which reduces the humidity difference between the air and the water surface. Furthermore, during the daytime, the net longwave radiation is usually positive, which can contribute to sea surface heating, but in this study the heating effect due to longwave radiation is offset by the high U_{10} in the open ocean.

Furthermore, in enclosed waters, nighttime cooling is less dominant than in open waters due to regional atmospheric conditions and land-sea wind effects. R_{shf} becomes less dominant at nighttime in enclosed waters due to the smaller air-sea temperature difference compared to open waters (Luo et al., 2022; Yang et al., 2023). Then, the nighttime R_{lhf} in enclosed waters is influenced by the land-sea wind pattern, which can increase the water vapor flux and maintain a relatively high R_{lhf} at nighttime (Hussein, 2022; Sun and Wu, 2021). However, this is different from Figure 13b,d, where the R_{lhf} is low at nighttime. This is due to the low wind speed, which causes the heat flux from the ocean to the atmosphere to decrease. Like open water, longwave radiation at night contributes to surface cooling, but in this study the cooling effect is not influential when U_{10} is low in enclosed water. Kang et al. (2024) added that this effect might also be modulated by regional cloud cover and atmospheric humidity.

Besides the impact of oceanic regimes, air mass advection from terrestrial areas near water may significantly affect R_{shf} and R_{lhf} due to temperature and humidity differentials (Chu et al., 2024). This may be another consideration, as the research area is close to land, especially the A2 and A3 sites. The diurnal variability of T_s has been shown to be a major driver of R_{lhf} amplitude (Yan et al., 2021), especially in semi-enclosed ocean areas such as the Java Sea. This aligns with the findings of Wang and Dickinson (2013), which indicated that downward longwave radiation in the ocean exceeds that over land, suggesting a negative R_{lf} at three sites (Figure 12d,e,). The land albedo exceeds that of the ocean, resulting in decreased surface radiative heating compared to the ocean. A reduction in surface albedo over land, due to land use changes, enhances radiative heating, which subsequently induces upward heating, attracting additional water vapor from the ocean and thereby increasing R_{lhf} in the ocean (Lofgren, 1995).

5. Conclusion

This study successfully modeled the influence of ΔT_c and ΔT_w on T_s in the Sunda Strait using a coupled current and wave model approach. It was found that the ΔT_c consistently contributed negatively with an average thickness of ~ 55 μm and a temperature difference of about -0.2°C, which varied diurnally and showed an influence on U_{10}. When U_{10} is low during the daytime, a significant thin ΔT_w is formed. However, increasing U_{10} leads to temperature homogenization due to turbulent mixing, with ΔT_c approaching a stable value of -0.1°C. In addition, the sea surface net heat flux shows a decreasing trend with respect to U_{10} with a predominance of heat loss at nighttime and high variability during the daytime due to shortwave radiation. Through two correction steps (U_{10} and diurnal), this study successfully transformed the T_b into an accurate T_s estimate by removing the influence of ΔT_c and ΔT_w. Compared to other models, the new model shows a high correlation between ΔT_{cw} and U_{10} up to 0.87 and can represent the dynamics of enclosed water such as the Java Sea, which has different responses compared to open water due to water type, wave influence, and wind speed. The SWH is identified as the primary control on the T_s differences between the sites. In contrast, current speed correlates positively with ΔT_w in the open ocean but inversely in enclosed seas. This study also confirms that T_s

is influenced by ocean energy balances that are sensitive to meteorological changes, particularly U_{10}, R_{sw}, R_{lw}, R_{lhf} and R_{shf}. In the future, this study can serve as a basis for developing more realistic air-sea fluxes parameterization schemes in other open and enclosed waters.

Acknowledgements

The authors would like to express their gratitude to the Education and Training Center, BMKG for the doctoral scholarship support, Maritime Meteorology Center, BMKG for providing computing access for data processing, Prof. Tingwei Cui from Sun Yat-sen University, Zhuhai for his guidance in the preparation of Figure 2a, Dwi Aprizal who assisted with the high-quality figure editing for this paper, and to Masayu for her assistence in creating Figure 13.

This study was conducted under the Education and Training Center, BMKG scholarship scheme in collaboration with IPB University, under contract number KP.02.00/05-TB/SU/I/2024.

Conflict of interest

None declared.

References

Alappattu, D.P., Wang, Q., Yamaguchi, R., Lind, R.J., Reynolds, M., Christman, A.J., 2017. *Warm layer and cool skin corrections for bulk water temperature measurements for air-sea interaction studies*. J. Geophys. Res. Oceans 122, 6470–6481. https://doi.org/10.1002/2017JC012688

Casey, K.S., Brandon, T.B., Cornillon, P., Evans, R., 2010. *The Past, Present, and Future of the AVHRR Pathfinder SST Program*. [in:] Barale, V., Gower, J.F.R., Alberotanza, L. (Eds.), *Oceanography from Space: Revisited*, Springer, Dordrecht, 273–287. https://doi.org/10.1007/978-90-481-8681-5_16

Chakraborty, K., Joshi, A.P., Ghoshal, P.K., Ghosh, J., Akhand, A., Bhattacharya, T., Sreeush, M.G., Valsala, V., 2023. *Mechanisms and drivers controlling spatio-temporal evolution of pCO_2 and air-sea CO_2 fluxes in the southern Java coastal upwelling system*. Estuar. Coast. Shelf Sci. 293, 108509. https://doi.org/10.1016/j.ecss.2023.108509

Chu, H., Cao, C., Wang, W., Xiao, W., Zhang, K., Zhang, M., Lee, X., 2024. *The Land Wet-Bulb Temperature Increases Faster Than the Sea Surface Temperature*. Geophys. Res. Lett. 51, e2023GL106617. https://doi.org/10.1029/2023GL106617

Cronin, M.F., Gentemann, C.L., Edson, J., Ueki, I., Bourassa, M., Brown, S., Clayson, C.A., Fairall, C.W., Farrar, J.T., Gille, S.T., Gulev, S., Josey, S.A., Kato, S., Katsumata, M., Kent, E., Krug, M., Minnett, P.J., Parfitt, R., Pinker, R.T., Stackhouse, P.W., Swart, S., Tomita, H., Vandemark, D., Weller, A.R., Yoneyama, K., Yu, L., Zhang, D., 2019. *Air-Sea Fluxes With a Focus on Heat and Momentum*. Front. Mar. Sci. 6. https://doi.org/10.3389/fmars.2019.00430

de Moura, C.A., Kubrusly, C.S., 2013. *The Courant–Friedrichs–Lewy (CFL) Condition 80 Years After Its Discovery*. Birkhäuser, 249 pp.

Donlon, C., Robinson, I.S., Wimmer, W., Fisher, G., Reynolds, M., Edwards, R., Nightingale, T.J., 2008. *An Infrared Sea Surface Temperature Autonomous Radiometer (ISAR) for Deployment aboard Volunteer Observing Ships (VOS)*. J. Atmos. Ocean. Technol. 25, 93–113. https://doi.org/10.1175/2007JTECHO505.1

Donlon, C.J., Minnett, P.J., Gentemann, C., Nightingale, T.J., Barton, I.J., Ward, B., Murray, M.J., 2002. *Toward Improved Validation of Satellite Sea Surface Skin Temperature Measurements for Climate Research*. J. Clim. 15, 353–369. https://doi.org/10.1175/1520-0442(2002)015<0353:TIVOSS>2.0.CO;2

Fairall, C.W., Bradley, E.F., Godfrey, J.S., Wick, G.A., Edson, J.B., Young, G.S., 1996a. *Cool-skin and warm-layer effects on sea surface temperature*. J. .Geophys. Res. Oceans 101, 1295–1308. https://doi.org/10.1029/95JC03190

Fairall, C.W., Bradley, E.F., Rogers, D.P., Edson, J.B., Young, G.S., 1996b. *Bulk parameterization of air-sea fluxes for Tropical Ocean-Global Atmosphere Coupled-Ocean Atmosphere Response Experiment*. J. Geophys. Res. Oceans 101, 3747–3764. https://doi.org/10.1029/95JC03205

Fernández, P., Speich, S., Borgnino, M., Meroni, A.N., Desbiolles, F., Pasquero, C., 2023. *On the importance of the atmospheric coupling to the small-scale ocean in the modulation of latent heat flux*. Front. Mar. Sci. 10, 1136558. https://doi.org/10.3389/fmars.2023.1136558

Ganeshan, M., Wu, D.L., 2016. *The open-ocean sensible heat flux and its significance for Arctic boundary layer mixing during early fall*. Atmos. Chem. Phys. 16, 13173–13184. https://doi.org/10.5194/acp-16-13173-2016

Gentemann, C.L., Minnett, P.J., 2008. *Radiometric measurements of ocean surface thermal variability*. J. Geophys. Res. Oceans 113. https://doi.org/10.1029/2007JC004540

Haryanto, Y., Agdialta, R., Hartoko, A., Anggoro, S., Zainuri, M., 2019. *Effect of the Monsoon to Sea Surface Temperature in the Java Sea*. [in:] *Proceedings of the International Conference on Maritime and Archipelago (ICoMA 2018)*, Atlantis Press, 86–89. https://doi.org/10.2991/icoma-18.2019.19

Hersbach, H., Bell, B., Berrisford, P., Hirahara, S., Horányi, A., Muñoz-Sabater, J., Nicolas, J., Peubey, C., Radu, R., Schepers, D., Simmons, A., Soci, C., Abdalla, S., Abel-

lan, X., Balsamo, G., Bechtold, P., Biavati, G., Bidlot, J., Bonavita, M., De Chiara, G., Dahlgren, P., Dee, D., Diamantakis, M., Dragani, R., Flemming, J., Forbes, R., Fuentes, M., Geer, A., Haimberger, L., Healy, S., Hogan, R.J., Hólm, E., Janisková, M., Keeley, S., Laloyaux, P., Lopez, P., Lupu, C., Radnoti, G., de Rosnay, P., Rozum, I., Vamborg, F., Villaume, S., Thépaut, J.-N., 2020. *The ERA5 global reanalysis*. Q. J. Roy. Meteor. Soc. 146, 1999–2049. https://doi.org/10.1002/qj.3803

Hsu, P.-C., 2022. *Evaluation of Wind and Solar Insolation Influence on Ocean Near-Surface Temperature From in Situ Observations and the Geostationary Himawari-8 Satellite*. Remote Sens (Basel). 14, (19), 4975. https://doi.org/10.3390/rs14194975

Huang, B., Liu, C., Banzon, V., Freeman, E., Graham, G., Hankins, B., Smith, T., Zhang, H.-M., 2021. *Improvements of the Daily Optimum Interpolation Sea Surface Temperature (DOISST) Version 2.1*. J. Clim. 34, 2923–2939. https://doi.org/10.1175/JCLI-D-20-0166.1

Hussein, M.M.A., 2022. *Relationship Between Latent Heat Flux and Sea Surface Temperature in Alexandria Eastern Harbor, Egypt*. Turk. J. Fish. Aquat. Sci. 22 (6), TRJFAS20642. http://doi.org/10.4194/TRJFAS20642

Iversen, S.C., Sperrevik, A.K., Goux, O., 2023. *Improving sea surface temperature in a regional ocean model through refined sea surface temperature assimilation*. Ocean Sci. 19, 729–744. https://doi.org/10.5194/os-19-729-2023

Jessup, A.T., Branch, R., 2008. *Integrated Ocean Skin and Bulk Temperature Measurements Using the Calibrated Infrared In Situ Measurement System (CIRIMS) and Through-Hull Ports*. J. Atmos. Ocean. Tech. 25, 579–597. https://doi.org/10.1175/2007JTECHO479.1

Kang, E.-J., Sohn, B.-J., Kim, S.-W., Kim, W., Kwon, Y.-C., Kim, S.-B., Chun, H.-W., Liu, C., 2024. *A revised ocean mixed layer model for better simulating the diurnal variation in ocean skin temperature*. Geosci. Model Dev. 17, 8553–8568. https://doi.org/10.5194/gmd-17-8553-2024

Komen, G.J., Hasselmann, S., Hasselmann, K., 1984. *On the existence of a fully developed wind-sea spectrum*. J. Phys. Oceanogr. 14, 1271–1285.

Li, Z., Guan, L., Chen, R., 2023. *Sea surface skin temperature retrieval from HY-1D COCTS observations*. Front. Mar. Sci. 10. https://doi.org/10.3389/fmars.2023.1205776

Lofgren, B.M., 1995. *Sensitivity of Land–Ocean Circulations, Precipitation, and Soil Moisture to Perturbed Land Surface Albedo*. J. Clim. 8 (10), 2521–2542. https://doi.org/10.1175/1520-0442(1995)008<2521:SOLCPA>2.0.CO;2

Luo, B., Minnett, P.J., Szczodrak, M., Akella, S., 2022. *Regional and Seasonal Variability of the Oceanic Thermal Skin Effect*. J. Geophys. Res. Oceans 127, e2022JC018465. https://doi.org/10.1029/2022JC018465

Minnett, P.J., 2003. *Radiometric measurements of the sea-surface skin temperature: the competing roles of the diurnal thermocline and the cool skin*. Int. J. Remote Sens. 24, 5033–5047. https://doi.org/10.1080/0143116031000095880

Minnett, P.J., Knuteson, R.O., Best, F.A., Osborne, B.J., Hanafin, J.A., Brown, O.B., 2001. *The Marine-Atmospheric Emitted Radiance Interferometer: A High-Accuracy, Seagoing Infrared Spectroradiometer*. J. Atmos. .Ocean Tech. 18, 994–1013. https://doi.org/10.1175/1520-0426(2001)018<0994:TMAERI>2.0.CO;2

Minnett, P.J., Smith, M., Ward, B., 2011. *Measurements of the oceanic thermal skin effect*. Deep Sea Res. Pt II, 58, 861–868. https://doi.org/10.1016/j.dsr2.2010.10.024

Murray, M.J., Allen, M.R., Merchant, C.J., Harris, A.R., Donlon, C.J., 2000. *Direct observations of skin-bulk SST variability*. Geophys. Res. Lett. 27, 1171–1174. https://doi.org/10.1029/1999GL011133

Olabarrieta, M., Warner, J.C., Kumar, N., 2011. *Wave-current interaction in Willapa Bay*. J. Geophys. Res. Oceans 116. https://doi.org/10.1029/2011JC007387

Pawlowicz, R., Beardsley, B., Lentz, S., 2002. *Classical tidal harmonic analysis including error estimates in MATLAB using T_TIDE*. Comput. Geosci. 28, 929–937. https://doi.org/10.1016/S0098-3004(02)00013-4

Pimentel, S., Tse, W.-H., Xu, H., Denaxa, D., Jansen, E., Korres, G., Mirouze, I., Storto, A., 2019. *Modeling the Near-Surface Diurnal Cycle of Sea Surface Temperature in the Mediterranean Sea*. J. Geophys. Res. Oceans 124, 171–183. https://doi.org/10.1029/2018JC014289

Pinker, R.T., Bentamy, A., Katsaros, K.B., Ma, Y., Li, C., 2014. *Estimates of net heat fluxes over the Atlantic Ocean*. J. Geophys. Res. Oceans 119, 410–427. https://doi.org/10.1002/2013JC009386

Putri, M.R., 2005. *Study of Ocean Climate Variability (1959–2002) in the Eastern Indian Ocean, Java Sea and Sunda Strait Using the HAMburg Shelf Ocean Model*. Ph.D. Dissertation, Hamburg Univ., 104 pp.

Saha, K., Zhao, X., Zhang, H., Casey, K.S., Zhang, D., Baker-Yeboah, S., Kilpatrick, K.A., Evans, R.H., Ryan, T., Relph, J.M., 2025. *AVHRR Pathfinder version 5.3 level 3 collated (L3C) global 4km sea surface temperature for 1981–2023*. NOAA National Centers for Environmental Information [www document].

Saunders, P.M., 1967a. *The Temperature at the Ocean-Air Interface*. J. Atmos. Sci. 24, 269–273. https://doi.org/10.1175/1520-0469(1967)024<0269:TTATOA>2.0.CO;2

Saunders, P.M., 1967b. *Aerial measurement of sea surface temperature in the infrared*. J. Geophys. Res. 72 (16), 4109–4117. https://doi.org/10.1029/JZ072i016p04109

Siregar, S., Yuliadi, L., Purba, N.P., Pranowo, W., Syamsuddin, M., 2017. *Pertukaran massa air di Laut Jawa terhadap periodisitas monsun dan Arlindo pada tahun 2015*. Depik 6, 44–59. https://doi.org/10.13170/depik.6.1.5523

Song, X., 2023. *Observed Opposite Fall-to-Winter Variations in the Air-Sea Latent Heat Flux Between the Western Boundary Currents and Coastal Seas*. Geophys. Res. Lett. 50, e2022GL100875. https://doi.org/10.1029/2022GL100875

Sun, X., Wu, R., 2021. *Seasonality and time scale dependence of the relationship between turbulent surface heat flux and SST*. Clim. Dynam. 56, 3173–3186. https://doi.org/10.1007/s00382-021-05631-0

Takaya, Y., Bidlot, J.-R., Beljaars, A.C.M., Janssen, P.A.E.M., 2010. *Refinements to a prognostic scheme of skin sea surface temperature*. J. Geophys. Res Oceans 115. https://doi.org/10.1029/2009JC005985

Tomita, H., Senjyu, T., Kubota, M., 2016. *Evaluation of air-sea sensible and latent heat fluxes over the Japan Sea obtained from satellite, atmospheric reanalysis, and objective analysis products*. J. Oceanogr. 72, 747–760. https://doi.org/10.1007/s10872-016-0368-y

Wang, K., Dickinson, R.E., 2013. *Global atmospheric downward longwave radiation at the surface from ground-based observations, satellite retrievals, and reanalyses*. Rev. Geophys. 51, 150–185. https://doi.org/10.1002/rog.20009

Ward, B., 2006. *Near-surface ocean temperature*. J. Geophys. Res. Oceans 111. https://doi.org/10.1029/2004JC002689

Willmott, C.J., Ackleson, S.G., Davis, R.E., Feddema, J.J., Klink, K.M., Legates, D.R., O'Donnell, J., Rowe, C.M., 1985. *Statistics for the evaluation and comparison of models*. J. Geophys. Res. Oceans 90, 8995–9005. https://doi.org/10.1029/JC090iC05p08995

Yan, Y., Wang, G., Wang, X.H., Chen, C., Ling, Z., Zhang, L., 2023. *Relationship between subsurface diurnal warming and wind speed*. Deep Sea Res. Pt. I, 199, 104106. https://doi.org/10.1016/j.dsr.2023.104106

Yan, Y., Zhang, L., Song, X., Wang, G., Chen, C., 2021. *Diurnal Variation in Surface Latent Heat Flux and the Effect of Diurnal Variability on the Climatological Latent Heat Flux over the Tropical Oceans*. J. Phys. Oceanogr. 51, 3401–3415. https://doi.org/10.1175/JPO-D-21-0128.1

Yang, M., Guan, L., Qu, L., Zhang, K., 2023. *Cool skin effect and warm skin phenomenon observed by shipboard radiometer in the Northwest Pacific*. Front. Mar. Sci. 10. https://doi.org/10.3389/fmars.2023.1212974

Yu, L., 2018. *Sea Surface Exchanges of Momentum, Heat, and Freshwater Determined by Satellite Remote Sensing*. [In:] Cochran, J.K., Bokuniewicz, H.J., Yager, P.L. (Eds.), *Encyclopedia of Ocean Sciences*, Vol. 1, 3rd Edn., Acad. Press, 15–23. https://doi.org/10.1016/B978-0-12-409548-9.11458-7

Zeng, X., Beljaars, A., 2005. *A prognostic scheme of sea surface skin temperature for modeling and data assimilation*. Geophys. Res. Lett. 32. https://doi.org/10.1029/2005GL023030

Zhang, H., Babanin, A.V, Liu, Q., Ignatov, A., 2019. *Cool skin signals observed from Advanced Along-Track Scanning Radiometer (AATSR) and in situ SST measurements*. Remote Sens. Environ. 226, 38–50. https://doi.org/10.1016/j.rse.2019.03.035

Zhang, H., Beggs, H., Ignatov, A., Babanin, A.V., 2020. *Nighttime Cool Skin Effect Observed from Infrared SST Autonomous Radiometer (ISAR) and Depth Temperatures*. J. Atmos. Ocean. Tech. 37, 33–46. https://doi.org/10.1175/JTECH-D-19-0161.1

Zhang, R., Zhou, F., Wang, X., Wang, D., Gulev, S.K., 2021. *Cool Skin Effect and its Impact on the Computation of the Latent Heat Flux in the South China Sea*. J. Geophys. Res. Oceans 126, 2020JC016498. https://doi.org/10.1029/2020JC016498